UAV Networks : Design Considerations

Abhinav Jadon

A thesis
submitted in partial fulfillment of the
requirements for the degree of

Master of Science in Electrical Engineering

University of Washington

2018

Reading Committee:

Sumit Roy, Chair

Payman Arabshahi

Program Authorized to Offer Degree:
Electrical Engineering

University of Washington

Abstract

UAV Networks : Design Considerations

Abhinav Jadon

Chair of the Supervisory Committee:
Integrated Systems Professor, Sumit Roy
Electrical Engineering

Unmanned Aerial Vehicles have come a long way, from starting out as military reconnaissance vehicles to a popular hobbyist's tool. Significant research and development efforts from the commercial drone industry have significantly improved commercial UAVs and has got the wireless network and communications design community thinking about the possibility of realization and deployment of UAV networks. UAV networks, if realized, offer a significant edge over conventional wireless communication networks, they can be easily re-configured and re-arranged to handle varying traffic, can provide critical communication facilities in disaster hit regions etc.

In this work, we explore the scenario where UAV air-to-ground communications between a low altitude platform such as a UAV flying happens over an open ground setting. An integral component of the above is to come up with a wireless channel model that depends more on physics rather than the empirical studies. Thus, this work develops a physics based wireless channel model for UAV air-ground link and validates the said model. This, to the best of the author's knowledge has never been attempted before. The authors then use the validated model to look for rate-based optimization as a UAV flies right above a ground node in a straight line.

TABLE OF CONTENTS

LIST OF FIGURES

GLOSSARY

See Fig. 2.8 for reference for some definitions below.
$h_1(h_2)$: height of Ground station (UAV) with reference to local ground plane
d: horizontal distance between Ground station and the UAV
γ: the angle of incidence
E_0: line-of-sight electric field component in free space
R_0: reflection coefficient of a smooth ground plane ≈ 1
$E_{r,2-ray}$: resultant deterministic electrical field at the receiver due to 2-ray model
ϕ: net phase shift between the direct and the wave reflected from the ground
δ: path difference between direct and specular wave
Φ: additive phase change due to ground reflection
λ: transmitted wavelength (corr. to carrier frequency)
$P_0(dBm)$: received power (dBm) corr. to E-field component E_0 in free-space
$P_t(dBm)$: transmitted power from source (dBm)
d_{LOS}: distance along ground plane between Tx and Rx
Δh is the standard deviation of normally distributed height variations
T is the horizontal auto-correlation distance
r is the distance from the transmitter to the receiver,
r_1 is the distance from the transmitter to the reflecting plane
r_2 is the distance from the reflecting plane to the receiver.
β_0 is defined as the tan inverse of the ratio of vertical and horizontal dimensions of irregularities
β is the angle made by the bisector of the incident and scattered rays with the z axis
δR_1 is the ratio of the reflected field to the incident field on the reflecting plane.
δR is the ratio of the reflected field to the incident field received by the same receiver.
δE_d is the diffused electric field at the receiver due to area element δS.
E_d is the diffused electric field received at the receiver.
ρ_d is the diffusion coefficient of the rough ground
E_r is the random variable for the electric field at the receiver.
σ^2 is the variance of the received electric field
K here represents the K factor for a Rician distribution
$E_{min,M}$ is the minimum electric field required at the receiver for decoding packets sent at rate M
$NoiseFloor$ is the noise floor at the receiver

$NoiseFigure$ is the noise figure of the receiver
$T_{thermal}$ is the temperature in kelvin
B is the bandwidth of transmission
k is the Boltzmann constant
$LAV_{h,M,x}$ is the link availability vector (binary); signifies the availability of the link at height h, rate M and horizontal distance x for a fixed system.
$RV_{h,x}$ is the rate vector; signifies the highest rate that can be achieved at height h and horizontal distance x for an adaptive system.
$CR_{h,M}$ is the contact range for height h and rate M. Contact Range is the range over which the UAV can communicate with the node on the ground.
$ADD - FR_{h,M}$ is the data that can be downloaded over the duration of contact range for a fixed rate system when the UAV flies at a height h and transmits at rate M.
$ADD - AR_h$ is the data that can be downloaded over the duration of contact range for a adaptive rate system when the UAV flies at a height h.

ACKNOWLEDGMENTS

The author wishes to express sincere appreciation to colleagues, friends, family and the University of Washington, without whom this dissertation might not have been possible, and to whom I am greatly indebted.

I thank my adviser, Prof. Sumit Roy, for his guidance and support through- out my graduate studies at University of Washington. His continuous encouragements for research and his invaluable advice has been an inspiration for my work.

I would like to thank my colleagues at Fundamentals of Networking Laboratory and fellow graduate students for the insightful discussions and for the quality time we spent together. This work is accomplished with the help of Farzad Hessar to whom I am very grateful.

Lastly, my deepest gratitude and thanks goes to my parents and my sister for their endless support and encouragement. They have always been my source of enthusiasm and inspiration throughout my life and I cannot express my appreciation in words.

DEDICATION

To my parents and my sister for their love and support

Chapter 1

INTRODUCTION

The scenario explored in this thesis is air-to-ground communications between a low altitude platform such as a UAV flying over an open ground setting. With the increasing availability of commodity drones (UAVs) equipped with radios operating typically over the unlicensed bands for UAV-UAV and UAV-GND node communications, there is considerable interest in feasible wireless network architectures that will be needed to support desired services and functions. Clearly, an integral component of the above is a re-visit of relevant wireless channel models and its implications for achievable rate/range trade-offs for UAV networks. Accordingly, a survey of the relevant prior art is first presented. While UAVs typically will fly over built human environments in urban settings at low altitudes [1], in this work we focus on flights over open areas - a simpler propagation scenario for the advantage it affords for insightful channel modeling. Further, channel measurement data collected as part of this (and other prior) efforts will support model validation and refinement. We construct a model for the received signal comprising of 3 components that accounts for propagation over a ground plane: a) a direct line-of-sight (LOS) ray, b) specular ground reflection and c) diffuse ground reflection, as derived from [1].

1.1 Discussion of Prior Art

UAV networks differ from terrestrial wireless networks in some fundamental ways - UAV nodes are subject to additional constraints that must be considered for network design. These constraints include battery life and form factor, flight time and path planning, and real-time time co-ordination between the aerial nodes among either [2, 3, 4]. These constraints are

[1] Current FAA regulations limit flight altitudes to below 400 ft.

often coupled with the radio propagation aspects that increase the complexity of overall network design. In this work, we begin ground up starting from characterizing the UAV Air-ground channel link.

UAV networks can be classified depending on their altitude - into HAPs (High Altitude Platforms) and LAPs (Low Altitude Platforms).

[5, 6, 7] detail the collection of HAP A-G link data and fitting distribution to the data to develop a model for the link variation with UAV parameters over different ground environments. All these studies are empirical in nature.

The LAP A-G link collection campaigns [8, 9, 10, 11, 12] have been limited to open space settings due to regulations on LAP flights in built areas. These campaigns are primarily empirical in nature and use data fitting to arrive at a model. Such channel models have been used by other researchers to come up with solutions to various network design and optimization problems [13, 14, 15, 16].

Purely analytical models for LAP A-G link in urban/semi-urban settings have also been developed in [17, 18, 19]. This line of work tries to develop propagation physics based models for UAV A-G link, as it provides key insights into network design not available from a purely empirical approach. A combination of physics-based modeling backed via empirical measurement data provides the right balance, and is undertaken in Chapter 2 deals (that develops an appropriate physics based model for LAP A-G link) and Chapter 3 that details on the data collection campaign and data processing.

Chapter 2

CHANNEL MODEL

Our approach to building the channel model is to analyze the different components of the signals - the direct wave, the specular component and the diffused component (as shown in Figure 2.1) separately and then superimposing them all together to obtain an expression for the resultant of the three. This gives us a channel model that provides much more insight on how the UAV air-ground link varies with height and distance from the ground node.
We assume that the reader is thoroughly acquainted with the nuances of direct wave and its propagation in space and thus skip discussing direct wave. We start by discussing specular component and then move on to diffused component.

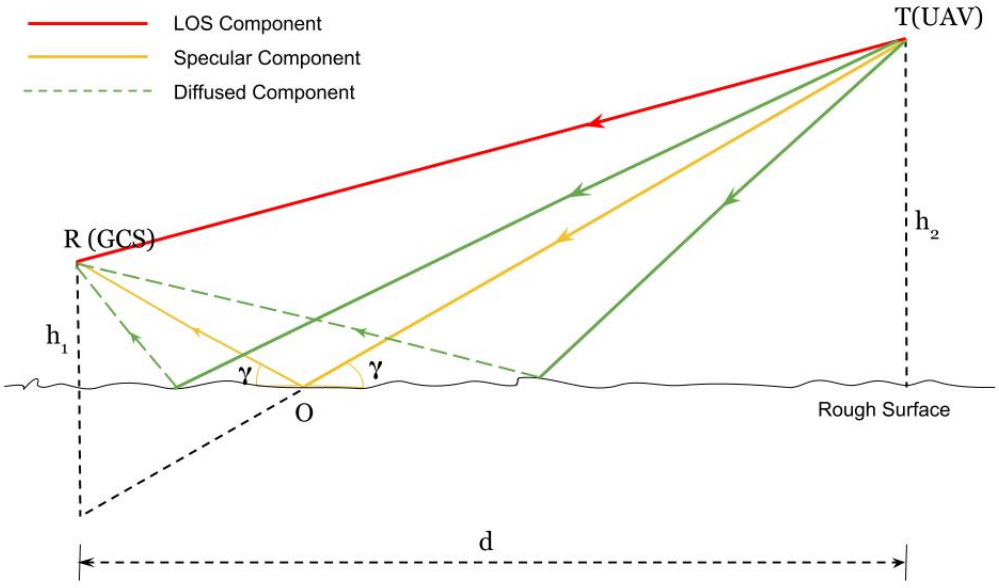

Figure 2.1: Geometry of the UAV air-ground radio link

2.1 Specular Component

In this section, we will introduce the specular component to the reader and then discuss its interaction with the direct wave. The figure below illustrates the link geometry.

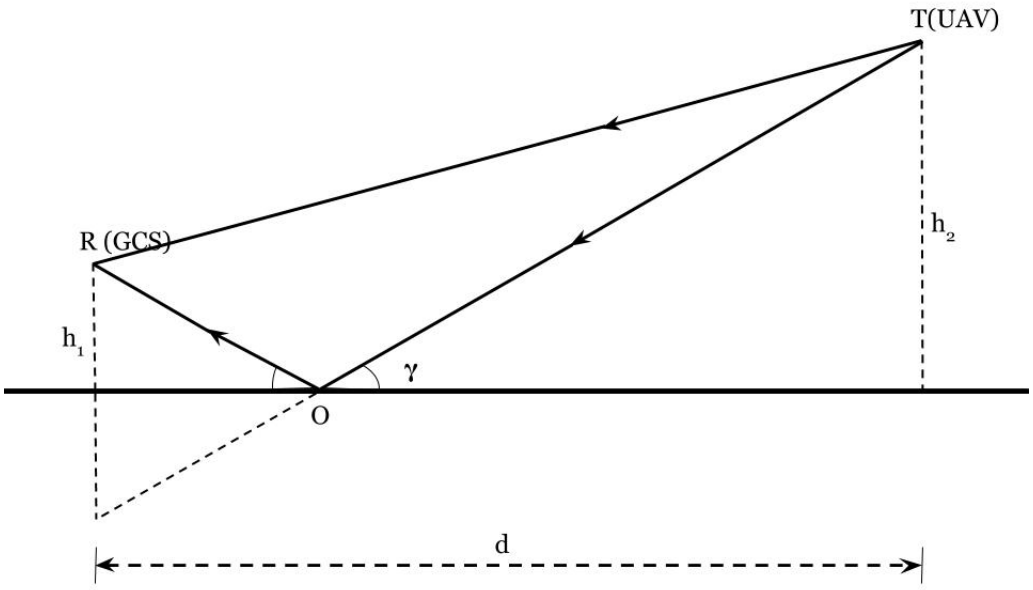

Figure 2.2: Geometry of the radio link considering only specular reflected and the LOS component

The amplitude of the resultant received E-field inclusive of the LOS and specular components, is given by:

$$E_{2-ray} = E_0\sqrt{(1+\mid R_0 \mid)^2 + 4 \mid R_0 \mid \cos^2 \phi/2} \tag{2.1}$$

where

$E_{r,2-ray}$: resultant deterministic electrical field at the receiver due to 2-ray model

E_0 is the LOS electric field component at the receiver in free space;

$\mid R_0 \mid$ is the magnitude of reflection coefficient of the perfectly smooth surface

ϕ is the net phase shift between the direct wave and the wave reflected from the ground, given by

$$\phi = 2\pi\delta/\lambda + \Phi \tag{2.2}$$

where

δ is the path difference between direct and reflected waves

Φ is the additional phase shift induced by ground reflection

λ is the wavelength corr. to the carrier frequency

It is easy to show that for $d >> h_1, h_2$

$$\delta = 2h_1h_2/d \tag{2.3}$$

We plot the ratio $E_{r,2-ray}/E_0$ vs. horizontal distance for various UAV heights h_2 (and fixed h_1).

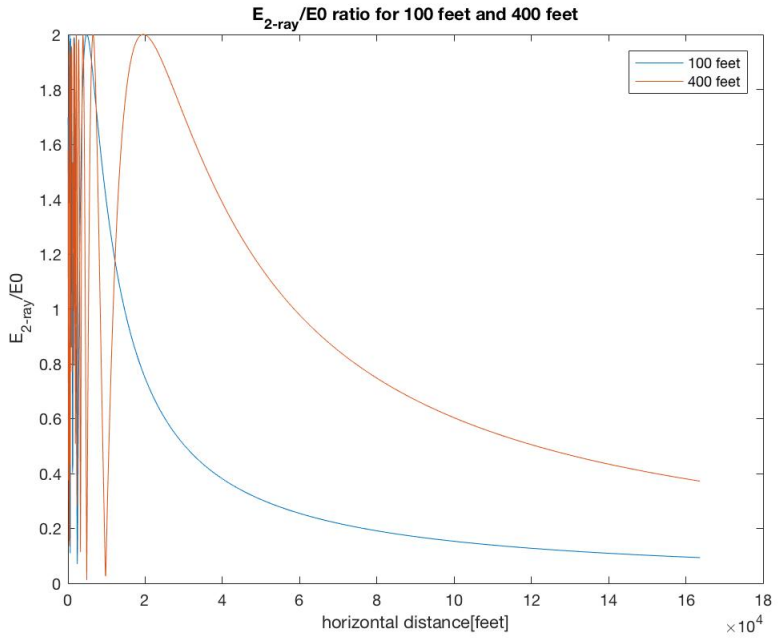

Figure 2.3: E_{2-ray}/E_0 variation with horizontal distance d for h_2= 100 feet and 400 feet, per Eq 2.1

Note that as the h_2 increases, the frequency of the fluctuations increase and level of the tail of the fluctuation also increases, as can be seen from (2.1).

Now

$$P_0(dBm) = P_t(dBm) - 10log_{10}(\frac{\lambda}{4\pi d_{LOS}})^2 \tag{2.4}$$

where
$P_0(dBm)$ is the free space received power in dBm
$P_t(dBm)$ is the transmitted power in dBm (30 dBm)
λ is the wavelength of the transmitted wave
d_{LOS} is the distance along the ground plane
and

$$E_0^2 = 10^{P_0(dBm)/10} \tag{2.5}$$

Using $\frac{E_{2-ray}}{E_0}$ ratio obtained in equation 1

$$E_{2-ray} = E_0 * \frac{E_{2-ray}}{E_0} \tag{2.6}$$

where
E_{2-ray} is the net mean received E-field amplitude

From (2.1) and (2.5), (2.6) can be written as

$$E_{2-ray} = \sqrt{10^{P_0(dBm)/10}}\sqrt{(1 + (\mid R_0 \mid)^2 + 4 \mid R_0 \mid \cos^2\phi/2} \tag{2.7}$$

The net received E-field amplitude with respect to the horizontal distance is plotted in Fig. 2.4.

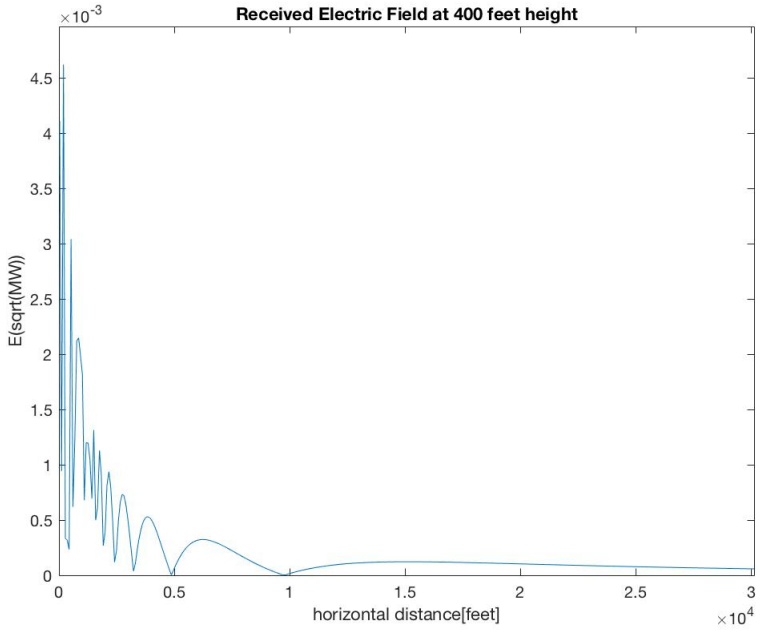

Figure 2.4: E variation with distance at height 400 feet; Equation 2.4 - 2.6

The above analysis provides a basic understanding as to how the specular component interacts with the LOS component to produce the mean-field resultant that varies with respect to horizontal distance. More details about the analysis can be found in [1], from which this heavily relies.

2.2 Diffused Component from Rough Ground Plane

We now focus on the diffused component of the received signal. The diffused component, unlike the specular component, is phase incoherent and constitutes the resultant off a larger surface as shown in Fig. 2.5.

In the said figure - the origin O corresponds to the point right below the UAV and R corresponds to the point right below the ground station.The elliptical area marked in the figure can be thought of as collection of small area elements δS.

In figure 2.5 and as shown in [1], the area element δS, located at co-ordinates (x,y), is

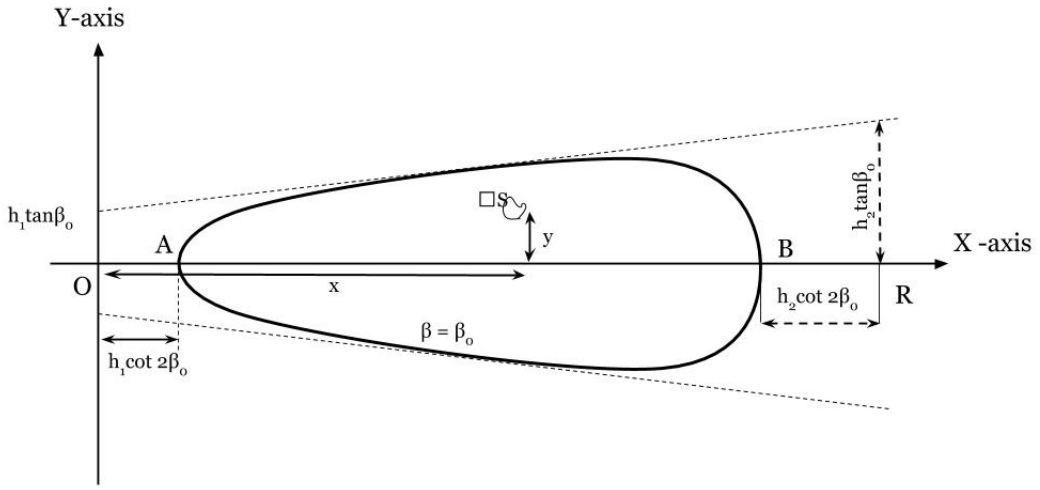

Figure 2.5: The area contributing to the diffused component of the reflected ray

chosen such that :

1. the area element is sufficiently small for incidence angle γ and the distance to the transmitter not to vary appreciably from one point on the element to another

2. the area element is large compared with the horizontal irregularities of the surface.

The area is bounded by the boundary defined by $\beta = \beta_0$ with β_0 given by

$$tan\beta_0 = \frac{2\Delta h}{T} \tag{2.8}$$

where

Δh is the standard deviation of normally distributed height variations and T is the horizontal auto-correlation distance.

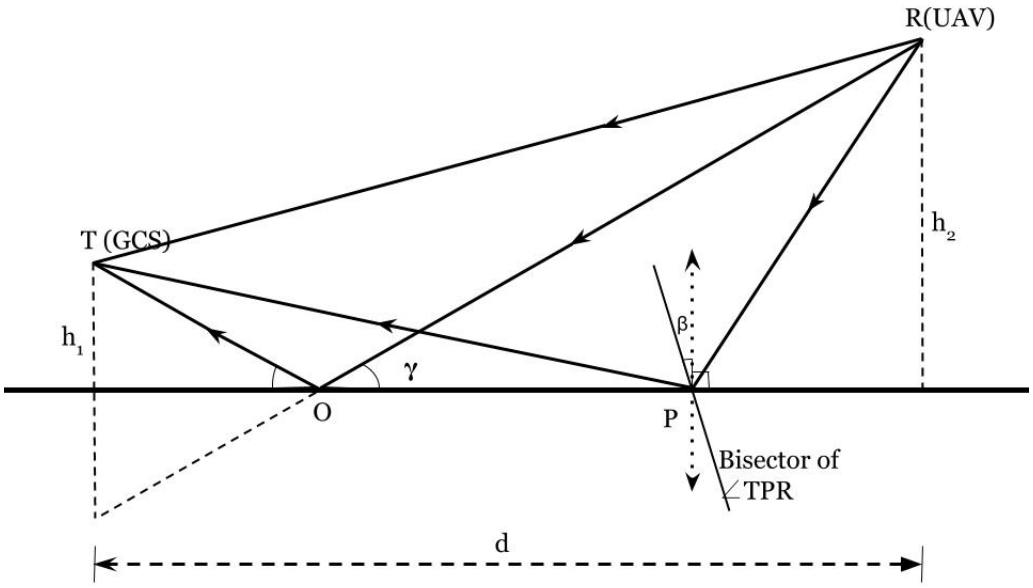

Figure 2.6: β shown in the link geometry context : Eq 16

The quantity β, as shown in Fig. 2.6 is the angle made by the bisector of the incident and scattered rays with the z axis. Point T is the Ground Control Station (GCS) and Point R is the position of the UAV.

It should be noted that the area contributing to the diffused component, depends on both the horizontal distance between and the heights of the UAV and the ground station. Fig. 2.5 suggests how the heights of the UAV and the ground station impact the size of the contributing area and hence the diffused component magnitude. The horizontal distance figures covertly in the β - as the horizontal distance between the nodes increasing, keeping all the other variables constant, the size of the contributing area decreases.

For a δS element in Fig 2.5, the mean square of the reflection coefficient δR_1 is given by [1],

$$<|\ \delta R_1\ |^2>= \frac{\cot^2\beta_0}{(\pi r_2^2 cos^4\beta)} \exp(-tan^2\beta/tan^2\beta_0)\delta S \tag{2.9}$$

where

β, as stated earlier, is the angle made by the bisector of the incident and scattered rays with the z axis

r_2 is the distance from the surface element δS to the receiver

For integrating over the area, T is assumed to be 1/3 times β_0

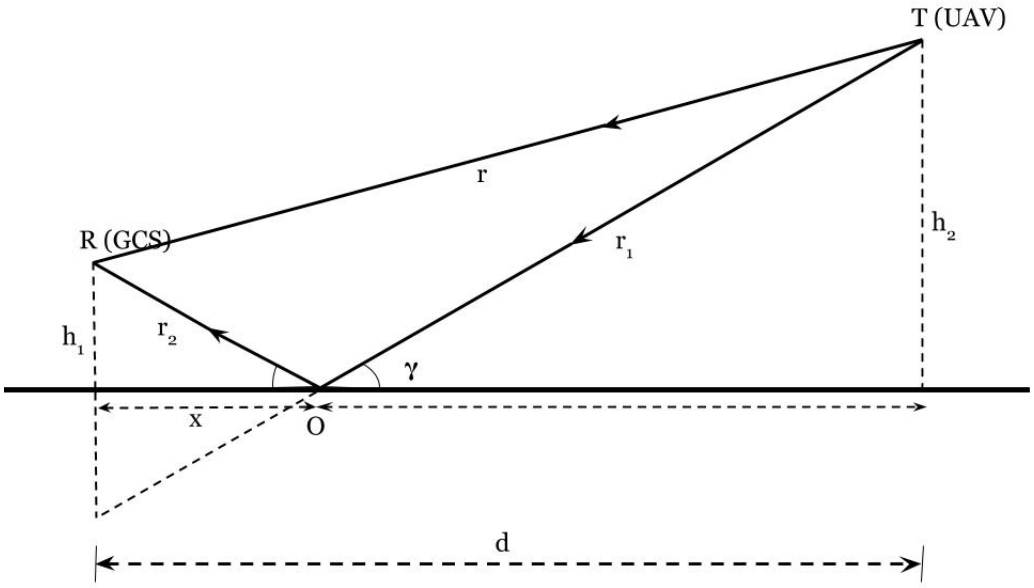

Figure 2.7: Link geometry with additional variables

The reflection coefficient δR_1 is defined as the ratio of the reflected field to the incident field on the area element δS.

Let δR be the ratio of the reflected field to the incident field received by the same receiver, then

$$\delta R = \delta R_1 \frac{r}{r_1} \tag{2.10}$$

where

r is the distance from the transmitter to the receiver,

r_1 is the distance from the transmitter to the reflecting plane

Thus, the expression for $< |\delta R|^2 >$ is defined as [1]:

$$< |\delta R|^2 >= \frac{r^2 \cot^2 \beta_0}{(\pi r_1^2 r_2^2 cos^4 \beta)} \exp(-tan^2\beta / tan^2\beta_0)\delta S \tag{2.11}$$

Ideally, the value of the reflection coefficient will be obtained by performing the integration over the area defined by β_0 but here, we consider only the elements lying along the horizontal line; accordingly the 1-dim. version of the above equation becomes,

$$< |\delta R|^2 >= \frac{r^2 \cot^2 \beta_0}{(\pi (h_1^2 + x^2)(h_2^2 + (d-x)^2) cos^4 \beta)} \exp(-tan^2\beta / tan^2\beta_0)\delta x \tag{2.12}$$

where

x is the horizontal distance between the transmitter and reflecting plane

The mean square of the field scattered by the surface of the earth is obtained by adding the mean squares of the fields scattered by the elements of the surface [1] :

$$< |E_d^2| >= \Sigma < \delta E_d >^2 \tag{2.13}$$

where

E_d is the diffused electric field seen at the receiver due to all the area elements

δE_d is the diffused electric field at the receiver due to an area element.

Assuming that the antennas are isotropic and also by the definition of δR given by (2.10),

$$< \delta E_d >^2 =< |\delta R|^2 > E_{2-ray}^2 \tag{2.14}$$

the mean square scattering coefficient, denoted by ρ_d, is then by (2.13) and (2.14) given by

$$< |\rho_d|^2 >= \Sigma < |\delta R|^2 > \tag{2.15}$$

Thus, by (2.13), (2.14) and (2.15)

$$< R_d^2 >=< |\rho_d|^2 > R_0^2 \tag{2.16}$$

For near smooth surfaces, the value of R_0 is close to 1, and

$$< R_d^2 >=< |\rho_d|^2 > \tag{2.17}$$

and for straight line AB in Figure 2.5, using (2.12) and (2.16)

$$< |\rho_d^2| >= \int_{h_1 \cot 2\beta_0}^{h_2 \cot 2\beta_0} \frac{r^2 \cot^2 \beta_0}{(\pi(h_1^2 + x^2)(h_2^2 + (d-x)^2) cos^4 \beta)} \exp(-\frac{tan^2 \beta}{tan^2 \beta_0}) \delta x \tag{2.18}$$

The expression of $< |\rho_d^2| >$ when the integration is done over the entire contributing region, can be found in Appendix A.

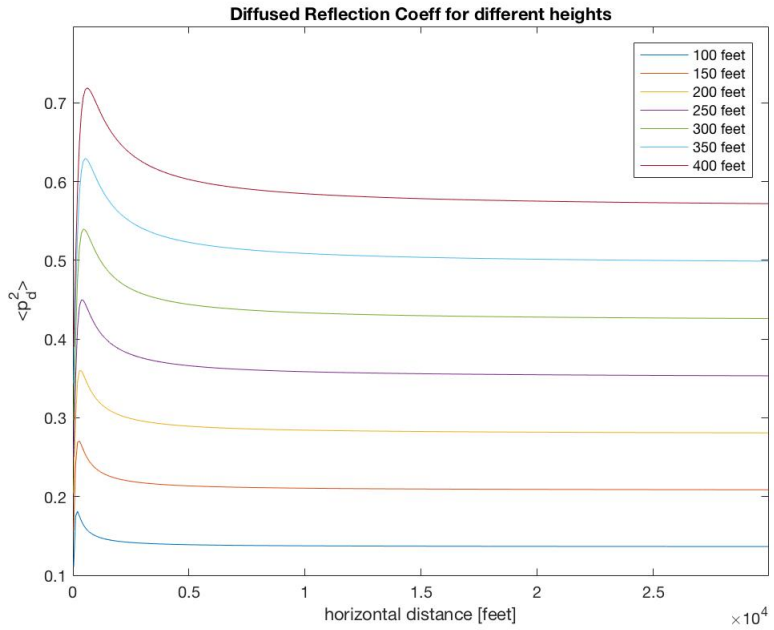

Figure 2.8: Variation of the $< \rho_d^2 >$ for a straight line : equation A.2

[1] cites the work of different authors, who by different experiments proved that both the specular and the diffused component exist for reflections bouncing off from rough surfaces, and that the diffused component is a Rayleigh distributed random variable. It is thus easy to see that the received electric field is a Rician distribution variable

$$E = E_{2-ray} + E_d \tag{2.19}$$

is a Rician distributed random variable since E_d - the electrical field of the diffused component is a Rayleigh distributed [1]. Therefore we have

$$E_d = X + jY \tag{2.20}$$

From (2.19) and (2.20), we get :

$$|E| = \sqrt{(E_{2-ray} + X)^2 + Y^2} \tag{2.21}$$

The diffused component superposed with the 2-ray deterministic model, which accounts for the specular component as discussed in the previous section, combines to produce a net E-field that is characterized by a Rician distribution of the form [1]

$$dP(\frac{|E|}{E_{2-ray}} > \epsilon) = \frac{2\epsilon}{< |\rho_d^2| >} exp(-\frac{1+\epsilon^2}{< |\rho_d^2| >}) I_0(\frac{2\epsilon}{< |\rho_d^2| >})\, d\epsilon \tag{2.22}$$

which can be re-written as

$$f_{|E|}(|e|) = \frac{|e|}{\sigma^2} exp(-\frac{|e|^2 + E_{2-ray}^2}{2\sigma^2}) I_0(\frac{E_{2-ray}|e|}{\sigma^2}) \tag{2.23}$$

where

E_{2-ray} is the mean E-field due to direct LOS and specular components

$\sigma^2 = E_{2-ray}^2 < |\rho_d^2| >/2$ is the variance of the distribution, and

$< |\rho_d^2| >$ is the reflection coefficient for the scattered component.

For notational ease, define $R = |E|$ and $v = E_{2-ray}$, then (2.23) is of the form

$$f_R(r) = \frac{r}{\sigma^2} exp(-\frac{r^2 + v^2}{2\sigma^2}) I_0(\frac{vr}{\sigma^2}) \tag{2.24}$$

A Rician distribution has a shape and scale parameters associated with it, the shape parameter K and the scale parameter Ω are defined as :

$$K = \frac{v^2}{2\sigma^2} \tag{2.25}$$

$$\Omega = v^2 + 2\sigma^2 \tag{2.26}$$

Using these two parameters, the distribution in (2.24) can be expressed in an alternate form as:

$$f_R(r) = \frac{2(K+1)r}{\Omega} exp(-K - \frac{(K+1)r^2}{\Omega}) I_0(2\sqrt{\frac{K(K+1)}{\Omega}} r) \;\; r,\, K,\, \Omega \;\geq\; 0 \tag{2.27}$$

We will use the above form throughout the document.

2.3 Variation of Rician Factor

As shown in the previous section, the net received E-field is Rician distributed with the distribution described in (2.24). The K factor of a Rician distribution is defined as the ratio of the power of the spectral component (mean) and the power of the scattered component :

$$K = \frac{v^2}{2\sigma^2} \tag{2.28}$$

where v is the mean and σ^2 the variance of the Rician distribution.
In this case, K factor for the received electric field distribution is given by :

$$K = \frac{E_{2-ray}^2}{< |\rho_d^2| > \; E_{2-ray}^2} = \frac{1}{< |\rho_d^2| >} \tag{2.29}$$

As can be seen from the equations in the previous section, K is not only a function of elevation angle but UAV height. Previous empirical works like [8] have not explored this dependence carefully, and only noted that K monotonically increases with elevation angle for fixed h_2.
Figure 2.9 shows the variation of K for different heights h_2 vs the elevation angle.

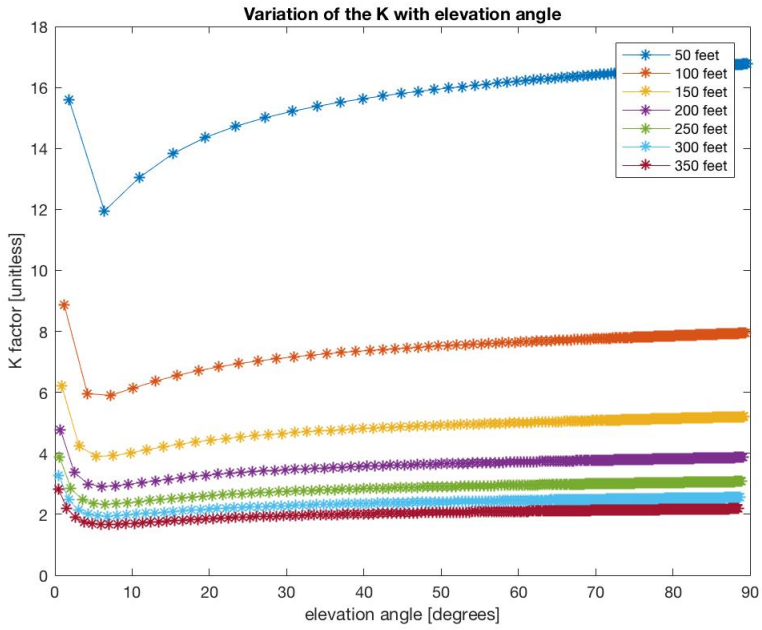

Figure 2.9: Variation of the K with elevation angle for different heights : (Eq 2.29)

As can be seen, the Rician Factor K initially decreases, and then monotonically increases for the remaining elevation angles. This is aligned with previous works [13] that have analytically claimed the existence of an optimized height which maximizes the coverage area if K is a monotonically increasing function.

The dip can be explained by the fact that for small angles, the diffused component is near negligible (as the size of the contributing area decreases and the surface can thus be assumed to be smooth) and the specular component is considerably lower in magnitude as well.

Chapter 3

DATA FITTING CHAPTER

3.1 Data Collection

Our Data collection campaign involved strapping Software defined radios(SDR) - capable of transmitting WiFi packets- to off the shelf UAV hardware and setting up a ground station where the SDR on the ground is listening for packets. At the ground station SDR, upon decoding each packet, the following quantities are logged in a file.

Logged Quantity	Remarks
Time stamp	Time the packet was received
Packet Number	Packet serial number
CRC check	result of the CRC check : PASS/FAIL
MCS	Modulation Scheme (802.11a standard)
Length	length of the packet
Amp	Amplitude of the received packet
Offset	physical layer offset (as defined in the 802.11a standard)

Table 3.1: Quantities logged during the run of the experiment

In our physical layer implementation, Amp for a packet is calculated by taking the RMS value of of the received signal at various times over the duration of the packet. Amp is thus equivalent to E, the received electrical field which is a combination of the LOS, spectral and diffused component as shown throughout Chapter 2.

3.1.1 BladeRF

Broadly, SDRs offer significant advantage over commercial radios that are hardwired and offer very little configurability, as they allow control over all layers of the networking stacks especially the lower ones (PHY and MAC). Specifically, they offer the benefits from channel selection, adaptive modulation and coding (MAC) as well transmission over a range of channel bandwidth. While there are several candidate SDR solutions, we selected the BladeRF boards - mainly because of its small form factor. Some other important technical specifications of BladeRF are given below in Table 3.2 :

Table 3.2: Specifications of the the bladeRF SDR board.

Operating Frequency	300MHz - 3.8GHz
Bandwidth	28MHz (max)
ADC	12-bit 40MSPS
DAC	16 bit 38.4MHz
Power	U SB/DC Jack
FPGA	115KLE Altera Cyclone 4E
Soft Processor	NIOS
Processor Clock frequency	200 MHz (max)
Cost	$650
Form Factor	5" by 3.5"

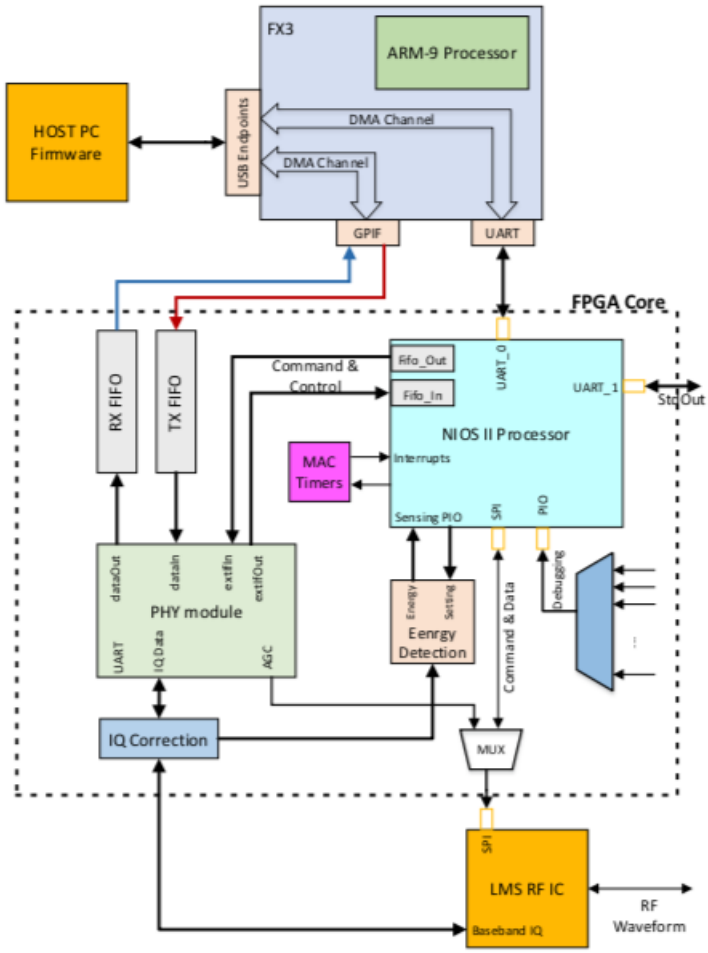

Figure 3.1: BladeRF architecture

The UW FUNLAB BladeRF platform consists of a BladeRF connected to a host computer. The host computer executes the code that frames the packets to be sent over the air. The packets are passed to the PHY module to be transmitted after processing. The host computer and the BladeRF are connected to each other via a USB link and the FX3 chip on BladeRF implements DMA channels to ensure fast transmission of packets from the

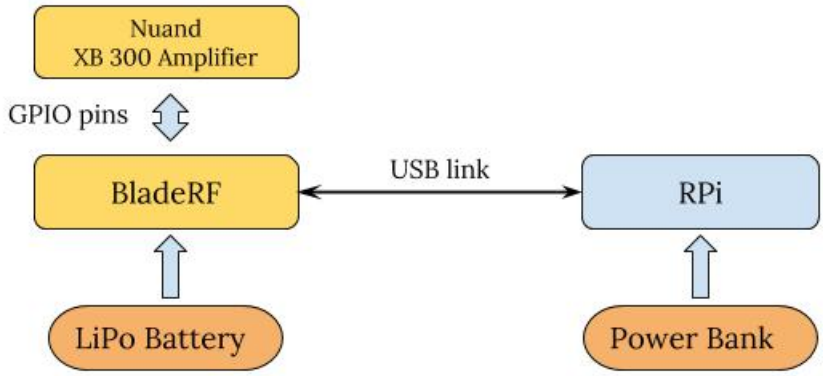

Figure 3.2: Block diagram of BladeRF system modified for mounting on UAVs

computer to the FPGA core, as shown in the Fig.3.1.
The PHY module on the FPGA processes the packets coming from the computer as per the 802.11a standard and transmits them over the air using the RF frontend (implemented on the BladeRF using LMS RF IC).

BladeRF board is mounted with an additional XB 300 amplifier card to increase the output transmit power (and hence down link range). The maximum TX power of the BladeRF board is 6 dBm (as shown in the table 3.2).
After adding the amplifier, the maximum TX power goes up to 36 dBm. As per FCC standards, the TX power of a device transmitting on the ISM band shouldn't exceed 30 dBm. Thus, the transmission power was set to not exceed the FCC limit.

Since amplifiers consume a lot of energy, the amplifier-BladeRF combine is powered using a LiPo battery. BladeRF is connected to a host computer(Raspberry Pi for UAV) that runs code responsible for framing packets and sends it down to the BladeRF using the USB 3.0

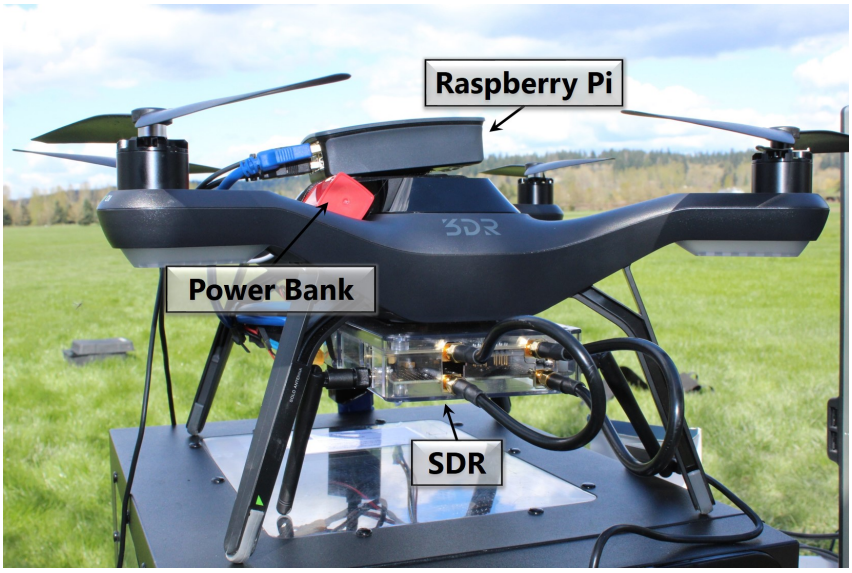

Figure 3.3: FUNLAB BladeRF platform mounted on a commercial drone

link.

3.1.2 Link Budget Analysis

Having discussed the hardware and its specs. We start with simple link budget analysis to get an estimate of the maximum possible distance between UAV node and ground node needed to ensure that the packet transmitted at 6 Mbps is decoded successfully. Table 3.3 lists the link budget parameters and their values.

For the values in Table 3.3, $Min\ RX\ power\ required\ = Noise\ Floor + Noise\ Figure + Min\ SNR\ required$ - $RX\ Amp\ gain$ - $RX\ antenna\ gain$

According to Link Budget formula (2.4) the maximum possible separation of UAV node and ground node for successfully decoding a 6 Mbps packet is given as :

$$d_{LOS} = \frac{\lambda(10^{(P_{TX}-P_{RX})/(\alpha*10)}}{(4\pi)} \tag{3.1}$$

where

d_{LOS} is the maximum possible separation between the UAV and ground node

P_{TX} is the TX power

P_{RX} is the minimum RX power required to decode 6 Mbps packets

α is the path loss exponent

λ is the wavelength of the transmitted signal

Plugging the parameters given in Table 3.3 in Equation 3.1, we get the maximum possible separation to be around $100m$ (approx 350 feet).

Table 3.3: Link Budget Parameters and their respective values

Link Budget Parameters	Values
Noise Floor (kTB) [Bandwidth = 6 MHz]	-106 dBm
Noise Figure	6 dB
Minimum SNR required (to decode 6 Mbps packets)	5 dB (conservative estimate)
TX power	30 dBm + 2 dBi = 32 dBm
RX antenna gain	2 dBi
RX Amp gain	30 dB
Path Loss Exponent	4
Minimum RX power required (at the decoder)	-95 dBm
Minimum RX power required (at the RF front end)	-123 dBm

For different rates, the maximum possible separation (d_{LOS}) will take different values as shown in table 3.4.

Table 3.4: Maximum Possible separation for different rates

Rates	d_{LOS}
6 Mbps	100 m
18 Mbps	75 m
54 Mbps	36 m

Since,

$$d_{LOS} = \sqrt{h^2 + x^2} \tag{3.2}$$

where

h is the height of the UAV

x is the horizontal distance between the UAV and the ground station

For fixed heights of 100 feet and 200 feet, the maximum horizontal distance possible is given by,

Table 3.5: Maximum possible horizontal distance for fixed heights

Rates	x [h=100 feet]	x [h = 200 feet]
6 Mbps	300 feet	260 feet
18 Mbps	225 feet	150 feet
54 Mbps	60 feet	N/A

3.1.3 Data Collection Methodology

We conducted experiments in open ground setting (e.g. Meadowbrook, North Bend). We flew the UAV to different pre-determined spots in space where it was made to hover for a certain duration of time until a sufficient number of packets were received. We covered six different heights starting from 50 feet to 300 feet with step of 50 feet and 3 different horizontal distances between the UAV and Ground Station, 100 feet, 200 feet and 300 feet.

At the end of the data collection campaign, we had data for around 20 points in space. No data was received at points that exceeded the link budget maximum separation (all the 300 feet height data). Apart from the link data we also managed to collect telemetry data that we think will be useful in the future if one were to understand how the UAV parameters such as pitch, yaw and tilt, to list a few, affect the link quality and availability.

This kind of analysis would only be possible if the telemetry data and the link data are both synchronized in time. We thus required some offline data processing to synchronize the two independent data streams. More details about the telemetry variables that were logged can be found in [20].

3.2 Data Processing

While a UAV is in flight, UAV telemetry parameters are logged on the UAV and the link data is logged at the ground station. The two data sets had to be synchronized using time stamps and organized into a database. While organizing the data into a database, we opted for a multi-table database design instead of a single integrated table as the link data is recorded at a much faster rate than the telemetry data. The user can then use a simple python script to extract data of interest in form <TimeStamp, Packet ID, Location, RX signal Amplitude, CRC result>

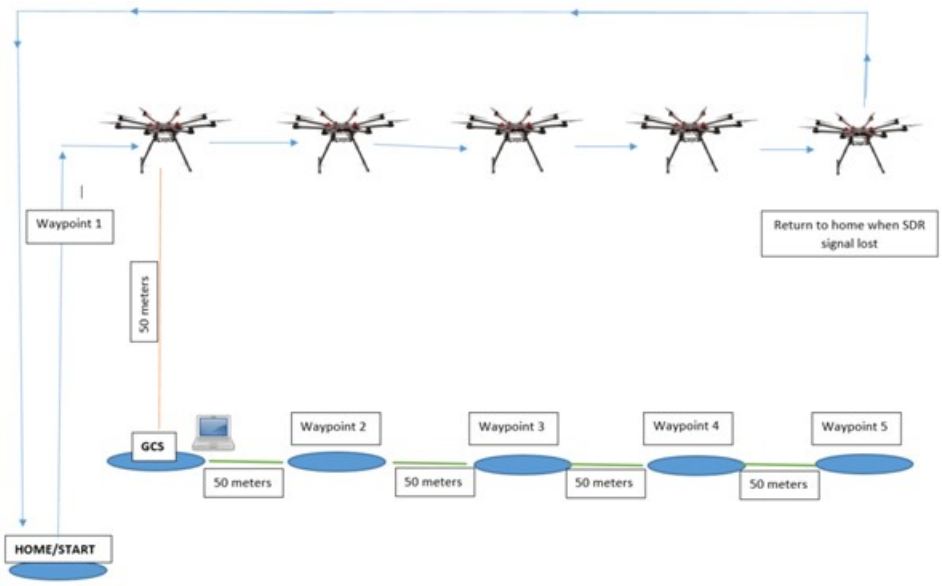

Figure 3.4: Flight way-points for data capture at a fixed height

A-G link datasets for low altitude UAVs do not appear to be readily available from prior efforts, the datasets collected from our trials have been uploaded and made accessible to the UAV research community. The link to the site (see Appendix B) and details regarding the associated data collection and database design effort is found in [20].

Collecting UAV link data is necessarily a time consuming effort, requiring significant set-up and logistical planning; as a result, we were only able to collect a sparse set (20 traces, each corresponding to a UAV location). Further, exerting control over environmental variables at run-time is difficult, resulting in spurious data elements at times. For example, the motion of people in the vicinity of the ground station impacts the downlink channel by creating additional specular components that lead to deviations from the predicted model parameters.

Figure 3.5: One of the flight testing sites. Meadowbrook Farm, North Bend, WA.

The above underscores the need to pre-process the data (data cleaning step) of potential spurious artifacts. Since there are only 20 traces, we chose to visually inspect the data for artifacts. Consider the trace in (Figure 3.6) - the data bounded by the red rectangle shows a mean value considerably different from the rest, and is removed.

After cleaning, each trace data was used to estimate the respective K factor of the Rician p.d.f at the corresponding UAV location.

Recall from Chap. 2, the net received E-field magnitude is represented by the Rician distribution of the form

$$f_R(r) = \frac{2(K+1)r}{\Omega} exp(-K - \frac{(K+1)r^2}{\Omega}) I_0(2\sqrt{\frac{K(K+1)}{\Omega}}r) \;\; r,\, K,\, \Omega \;\geq\; 0 \qquad (3.3)$$

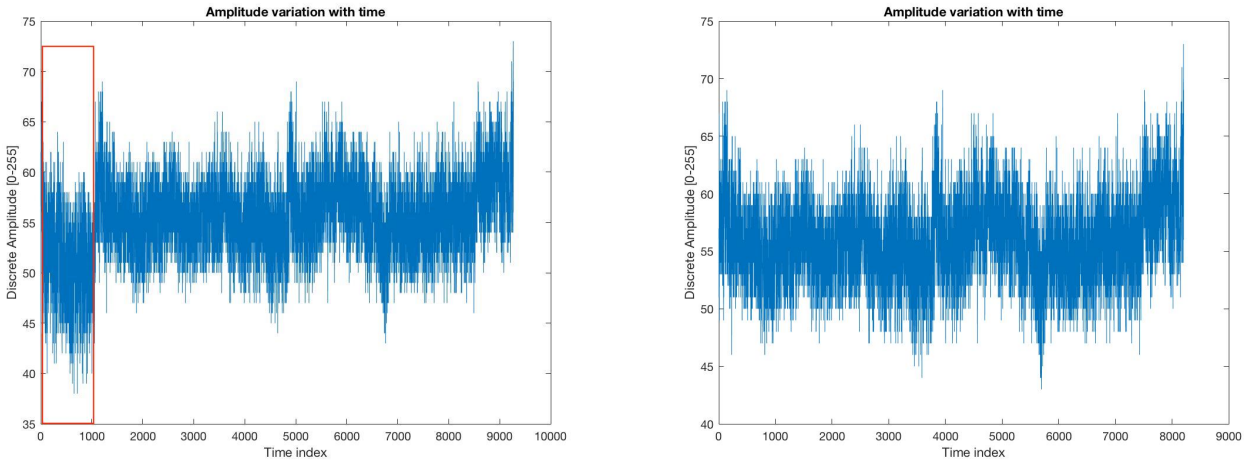

(a) Data trace from a point

(b) Data trace after cleaning

Figure 3.6: Data cleaning example

In [21], two moment based estimators of K are defined based on the following definitions: $\mu = E[R]/\sqrt{E[R^2]}$ and $\gamma = Var.[R^2]/\left(E[R^2]\right)^2$ where $E[.], Var.[.]$ represent the expectation and variance of the variable in the argument, resp. It is known that both μ, γ *depend only on* K and hence may be used to develop moment based estimators; of these γ is preferred as its relation to K is straightforward (less computational complexity), given by $\gamma = \frac{2K+1}{(K+1)^2}$ [1]. Hence

$$K = \frac{\sqrt{(1-\gamma)}}{1-\sqrt{(1-\gamma)}} \tag{3.4}$$

The estimator is then $\hat{K} = \frac{\sqrt{(1-\hat{\gamma})}}{1-\sqrt{(1-\hat{\gamma})}}$ where

$$\widehat{\gamma} = \frac{\widehat{Var[R^2]}}{\left(\widehat{E[R^2]}\right)^2} \tag{3.5}$$

where the respective sample estimators are $\widehat{Var[R^2]} = \frac{1}{n}\sum_i R_i^4 - \left(\frac{1}{n}\sum_i R_i^2\right)^2$ and $\widehat{E[R^2]} = \frac{1}{n}\sum_i R_i^2$. Hence

[1] According to [21], the performance of these estimator deviates from Cramer-Rao Lower Bound only slightly.

$$\widehat{\gamma} = \frac{\frac{1}{n}\sum_i R_i^4 - \left(\frac{1}{n}\sum_i R_i^2\right)^2}{\left(\frac{1}{n}\sum_i R_i^2\right)^2} \tag{3.6}$$

After cleaning the data, we plotted the K values from 12 different data sets. These data sets correspond to 4 different UAV heights : 50 feet, 100 feet, 200 feet and 250 feet and over 3 different horizontal UAV positions : 100 feet, 200 feet and 300 feet.

The x-axis of the graph is the horizontal distance between the UAV and ground station. The y axis of the graph is the K factor. It can be easily seen that our data also proves that K increases with increase in elevation angle for a fixed height.

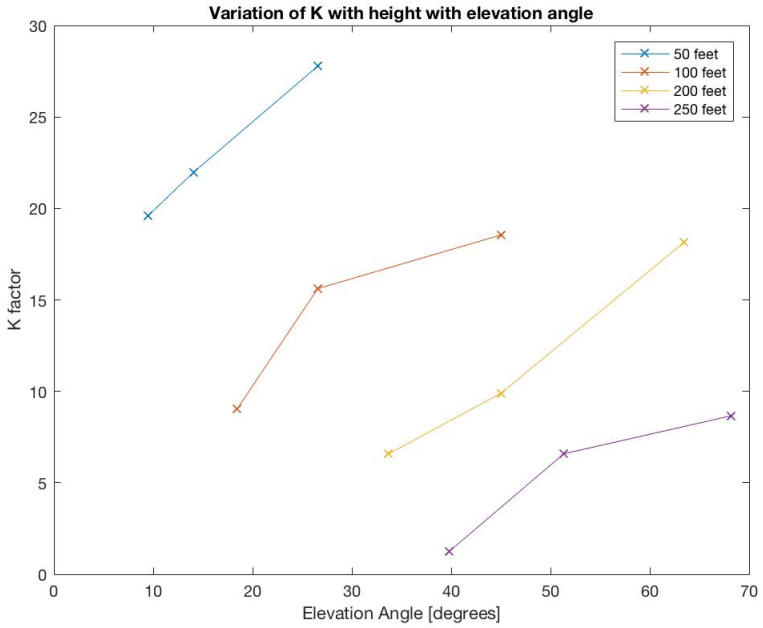

Figure 3.7: Variation of K with position of UAV as per collected data

Comparing the theoretical K factor values with the K factor values obtained after data cleaning in Table 3.6

UAV height[feet]	horizontal dist[feet]	theta[degrees]	K factor[Theory]	K factor[Data]
50	100	26.5	15	27.7
50	200	14	13.83	22
50	300	9.5	13.04	19.6
100	100	45	7.5	18.55
100	200	26.5	7	15.62
100	300	18.43	6.7	9.02
200	100	63	3.73	18.14
200	200	45	3.6	9.89
200	300	33.69	3.5	6.5
250	100	68	2.9	8.6
250	200	51	2.8	6.5
250	300	40	2.7	1.2

Table 3.6: Comparison of theoretical and real K factor values

One can see that while the trends align - the K factor for both the cases increases with increase in elevation angle - there are significant differences in the values.
The differences in values can be attributed to running the experiments in an uncontrolled environment coupled with the use of a simple data cleaning approach.In an uncontrolled environment, there are various factors that can add noise to the data. For our case, movement of people near the ground station was one of the major factors.

Chapter 4

BUILDING ON THE MODEL: SYSTEM DESIGN CONSIDERATIONS

The previous chapters described a physics based UAV air-to-ground (A-G) channel model and validated it using data from real experiments. In this chapter, we use the model to explore various optimization aspects for the UAV air-ground networking. We consider various aspects such as link availability (as a function of rate and height) and consequent link rate optimization, given the fact that UAVs are equipped with high-end sensors (notably cameras) with the main objective of streaming such data down to a (ground) control station for real-time navigation. While the joint path planning/navigation and A-G link design problem is the objective of final consequence, in this work we lay some initial foundations by considering a simple scenario: a single UAV flies directly over the ground node in a straight line at a fixed altitude.

4.1 Link Rate

In the earlier chapters, the A-G link rate has been shown to be a function of the position of the UAV with respect to the ground node, and the MCS rates that the UAV supports. We assume that the UAV uses legacy WiFi (802.11a) to connect to the ground node using a channel bandwidth of 20MHz, and we next map the .11a rates/MCS achievable as a function of altitude h and horizontal distance x.

To do the above, we express the electric field amplitude corresponding to minimum SNR required to decode packets encoded at rate M (for any MCS), as follows:

$$E^2_{min,M} = 10^{\frac{minSNR_M + NoiseFloor + NoiseFigure}{10}} \tag{4.1}$$

where

$E_{min,M}$ is the minimum electrical field required at the receiver to successfully decode the incoming packet coded with MCS rate M, $minSNR_M$ is the minimum SNR in dB, required at the receiver, $NoiseFigure$ quantifies the additional noise introduced by receiver components in dB and $NoiseFloor$ is the thermal noise floor of the receiver in dB, calculated using $10log_{10}(kTB)$ where k is the Boltzmann Constant, T is the Temperature in deg. Kelvin and B is the channel bandwidth.

For our analysis, we assume that the Noise Figure value is 6 dB, in line with typical noise figures seen in commercial wireless radios. Thus f the different MCS rates given by legacy WiFi, the minimum SNR required - defined in the standard - and the minimum electric field required to successfully decode the packet transmitted at that MCS (obtained from (4.1)) are given by Table 4.1 below.

MCS Index	MCS (Mbps)	Min SNR Required (dB)	min Elec Field Amp required(N/C)
0	6 Mbps	5	0.0317e-03
1	9 Mbps	6	0.0355e-03
2	12 Mbps	7	0.0399e-03
3	18 Mbps	9	0.0502e-03
4	24 Mbps	13	0.0795e-03
5	36 Mbps	17	0.1260e-03
6	48 Mbps	20	0.1780e-03
7	54 Mbps	22	0.2241e-03

Table 4.1: MCS,corresponding minimum SNR required and minimum electric field required to decode packets for a Noise Figure of 6 dB. via Eq. 4.1

Superimposing these on the graphs of received electrical field for UAV height 400 feet yields :

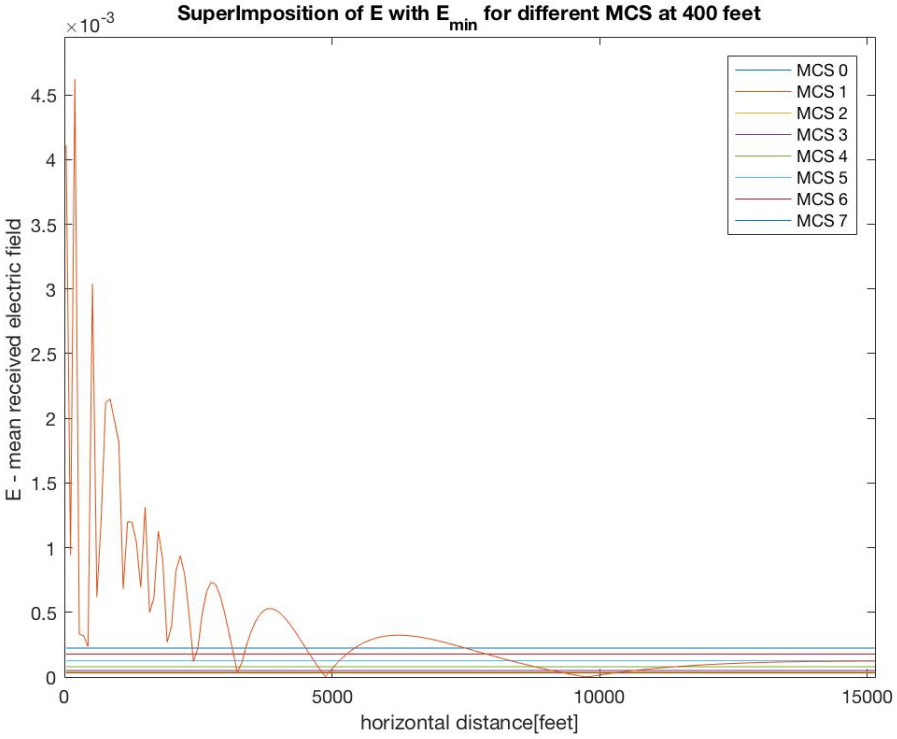

Figure 4.1: Superimposition of mean electrical Field at 400 feet height, with the minimum E levels corresponding to the SNR thresholds for different MCS

Looking at the Figure 4.1 it is clear the E-field fluctuations will not only lead to fluctuations in instantaneous A-G link rates but will also create 'holes' in the coverage for any fixed rate. We thus embark on quantifying the effect of these fluctuations next.

4.2 Link Availability Vector

For a UAV flying at a fixed height over a ground node with *fixed rate modem*, we define Link Availability Vector (LAV) that helps visualize the existence of 'holes' in coverage for a fixed MCS and height. Now, using the channel model developed earlier, the net received E-field amplitude (consisting of a direct LOS component, an indirect specular component

and Rayleigh distributed diffused component) is Rician distributed, with p.d.f given by

$$f_{|E|}(|e|) = \frac{|e|}{\sigma^2} exp(-\frac{|e|^2 + E_{2-ray}^2}{2\sigma^2}) I_0(\frac{E_{2-ray}|e|}{\sigma^2}) \tag{4.2}$$

where

E_{2-ray} is the mean E-field due to direct LOS and specular component, $\sigma^2 = E_{2-ray}^2 < |\rho_d^2| > /2$ is the variance of the distribution and and $< |\rho_d^2| >$ is the reflection coefficient for the scattered component.

For a Rician distribution, define the Marcum Q function (Q_1) as :

$$Q_1(a, b) = \int_b^\infty x exp(\frac{-(x^2 + a^2)}{2}) I_0(ax) dx \tag{4.3}$$

where a and b are non-negative real numbers, and I_0 is the modified Bessel function of the first kind of zero order.

We use the Q_1 to determine the link availability at every point within the coverage area. This is done by calculating at what UAV locations does the random received electrical field amplitude $|E|$ at the ground node exceed the $E_{min,M}$ 99.99 % of the time. The above translates to the LAV as follows:

$$LAV_{h,M,x} = \begin{cases} 1, & \text{if } Q_1(\frac{\sqrt{2}}{< \rho_d >}, \frac{\sqrt{2} E_{min,M}}{< \rho_d > E_{2-ray}}) > 0.9999 \\ 0, & \text{otherwise} \end{cases}$$

where $LAV_{h,M,x}$ is the binary vector for availability for a height h and MCS M, $E_{min,M}$ is the minimum electrical field value required at the receiver to decode at packet encoded with MCS M and x is the horizontal distance.

From the above equation, we can get LAV Maps for all the MCS listed in Table 4.1 and are given in Figure 4.2 and Figure 4.3.

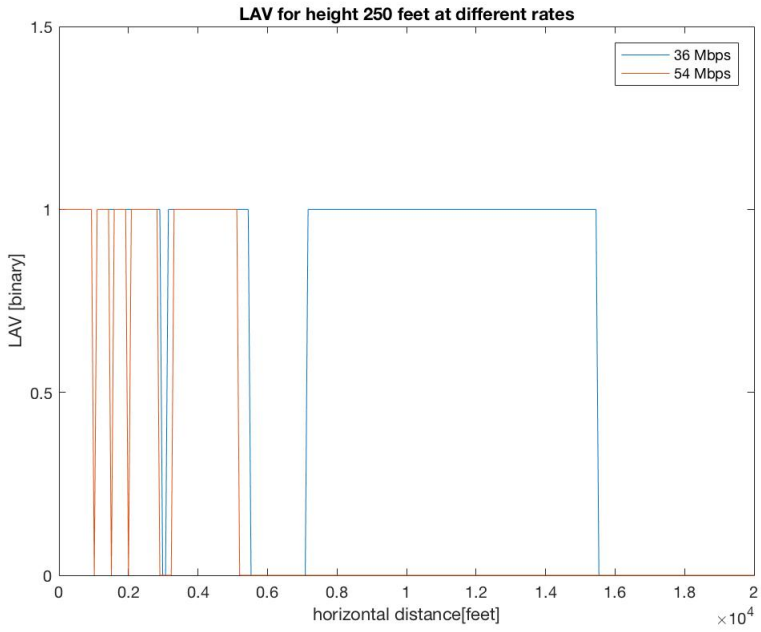

Figure 4.2: LAV for height 250 feet at different rates

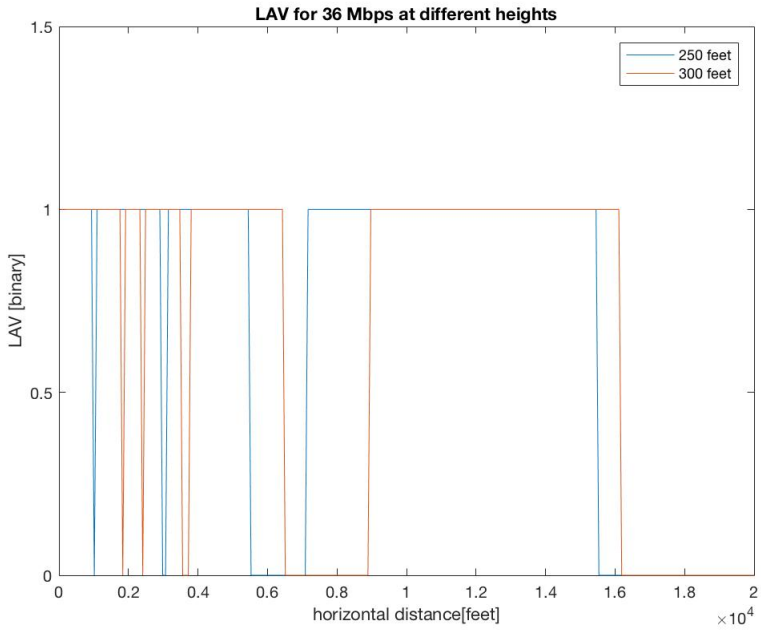

Figure 4.3: LAV for 36 Mbps at different heights

4.3 Rate Vector

Rate Vector assumes that the system has perfect adaptive modulation coding capability. Mathematically,

$$RV_{h,x} = \max(M * LAV_{h,M,x}) \texttt{over all values of M for a particular h and x} \quad (4.5)$$

where

$RV_{h,x}$ is the Rate Vector for height h, $LAV_{h,M,x}$ is the LAV for height h and rate M, and x is the horizontal distance. Rate Vector for height 400 feet is given in Figure 4.4 .

4.4 Contact Range

We define contact range (CR) as the maximum distance up til which the node and the UAV can maintain connectivity for a given MCS. Mathematically, it can be expressed as :

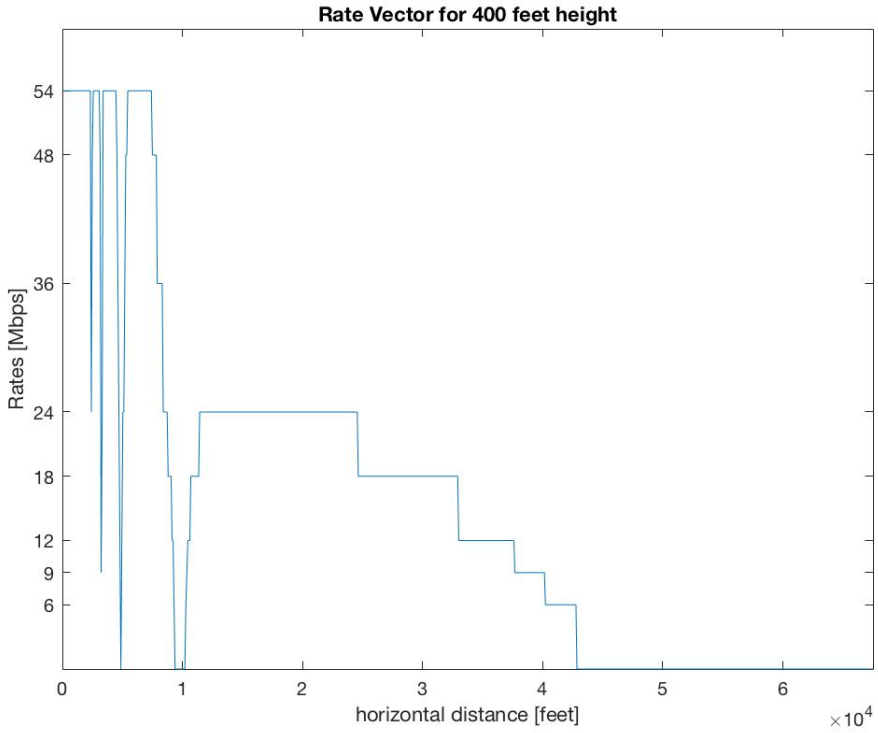

Figure 4.4: Rate Vector for height 100 feet. Eq 4.5

$$CR_{h,M} = (max(LAV_{h,M,x} = 1))\texttt{over all values of x for a particular h and M} \tag{4.6}$$

where

$LAV_{h,M}$ is the LAV (binary vector) for height h and rate M and x is the horizontal distance. As can be seen in Figure 4.2 and Figure 4.3, for both MCS rate, there exists a maximum distance after which the LAV is uniformly zero. This can be easily generalized to all the MCS rates.

The Figure 4.5 shows the variation of CR with UAV height at different rates. It should be noted that the Contact Range increases with increasing height, this can be attributed to the fluctuations of the specular component. With increasing height, as stated earlier in (2.1),

the frequency of the fluctuation is increases. This is shown in Chapter 2 in Figure 2.3.

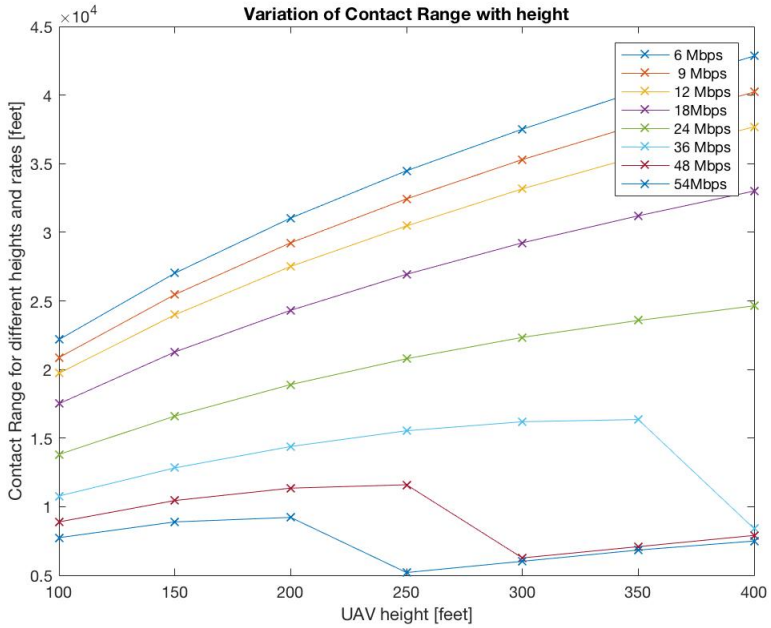

Figure 4.5: Variation of CR with UAV height for different rates Equation 4.6

However, as shown in Figure 4.5, this doesn't hold true for all the rates. For instance, for 54 Mbps, the contact range abruptly drops and then rises again. Plotting received electric field for heights 200 feet, 250 feet and 300 feet and superimposing it with the minimum electric field, we get Figure 4.6.

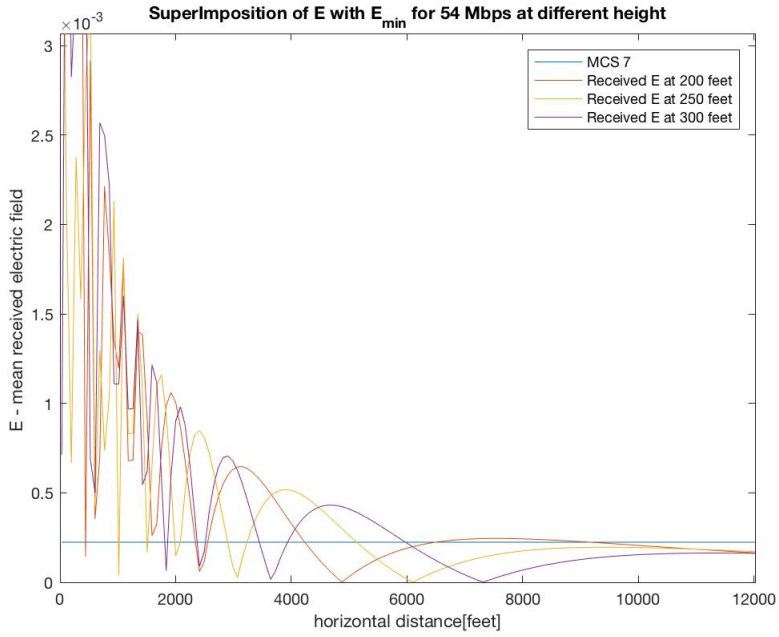

Figure 4.6: Superimposing received electric field for different height with the minimum level required for 54 Mbps

Looking closely at Figure 4.6, one can see that while it is the larger distance in case of height 250 feet that causes the electric field to drop below the required level. The contact range rebounds for 300 feet because of increased level of fluctuation with increase in height.

The Figure 4.7 shows the variation of CR with MCS rates at different UAV heights.

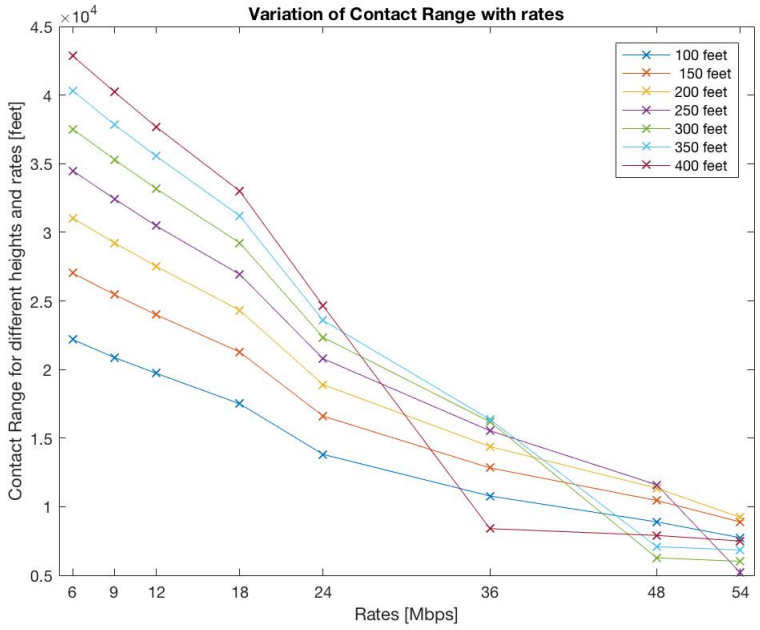

Figure 4.7: Variation of CR with rates at different heights Equation 4.6

Table 4.2 tabulates the values of contact range for different rates and heights.

UAV Height[feet]/MCS Rate[Mbps]	100 feet	150 feet	200 feet	250 feet	300 feet	350 feet	400 feet
6 Mbps	2.2178	2.7018	3.1037	3.4482	3.7516	4.0305	4.2848
9 Mbps	2.0866	2.5459	2.9232	3.2431	3.5302	3.7844	4.0223
12 Mbps	1.9718	2.3983	2.7510	3.0463	3.3169	3.5548	3.7680
18 Mbps	1.7503	2.1276	2.4311	2.6936	2.9232	3.1201	3.3005
24 Mbps	1.3812	1.6601	1.8898	2.0784	2.2343	2.3573	2.4639
36 Mbps	1.0778	1.2828	1.4386	1.5535	1.6191	1.6355	0.8399
48 Mbps	0.8891	1.0449	1.1352	1.1598	0.6266	0.7087	0.7907
54 Mbps	0.7743	0.8891	0.9219	0.5200	0.6020	0.6841	0.7497

Table 4.2: Contact Range values for different heights and Rates. All contact range values are in 10^4 feet

4.5 Aggregate Data Downloaded (Fixed Rate)

Let us assume that the fixed wing UAV is flying at a constant speed of v feet/s and is capable of transmitting at one of the fixed rates only (given in Table 4.1). Further, the flying speed is low enough for us to ignore the impact of Doppler effects on link quality. Aggregate data downloaded for a particular height and MCS in that case, is given as

$$ADD - FR_{h,M} = \sum_{x} \frac{2 * LAV_{h,M,x} * M}{v} \tag{4.7}$$

where
M is the MCS rate
$ADD - FR_{h,M}$ is the aggregate data download for that particular height and MCS
$LAV_{h,M,x}$ is the Link Availability Vector (binary vector) for that particular height and MCS
v is the speed of the UAV in feet/s

A reasonable estimate of UAV speed is around 0.25 m/s (0.82 feet/s). In our simulations, we assumed $v = 1$ feet/s for ease in scaling the ADD-FR values for different speeds. After simulations,we obtain Figure 4.8
As one can see, the data downloaded is maximized in a fixed rate setting for a particular MCS rate. The maxima is achieved at 18 Mbps for heights 300 feet, 400 feet, 500 feet. The maxima for heights 100 feet and 200 feet is achieved at 48 Mbps and 36 Mbps respectively. For some heights, the ADD-FR drops abruptly before climbing up again, this can be attributed to the fluctuation of contact range discussed in contact range section.

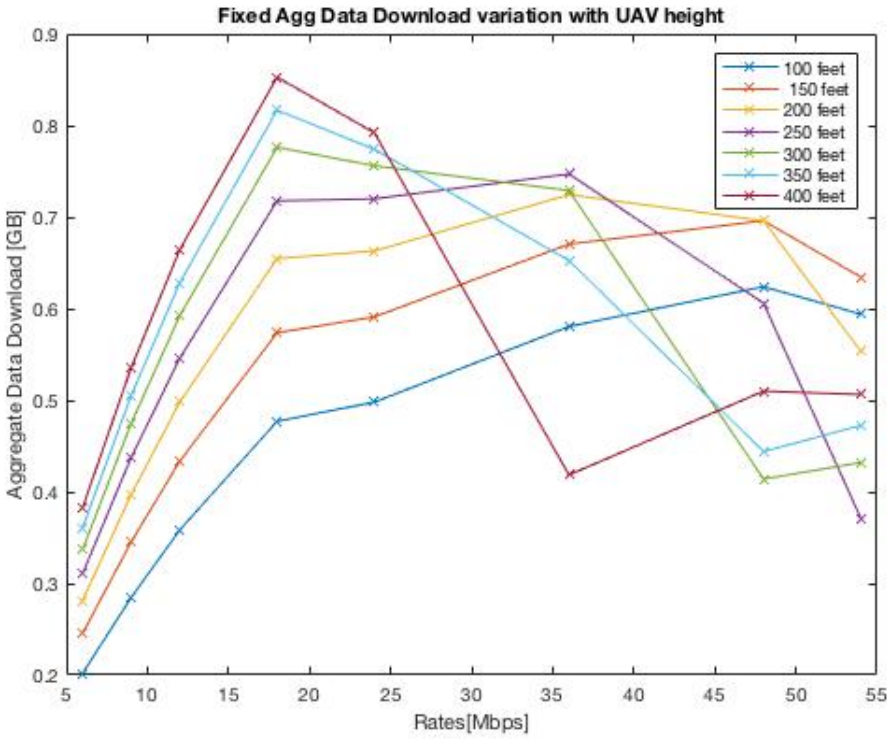

Figure 4.8: Agg. Data Downloaded variation over different MCS at different UAV heights in a fixed rate scenario. Eq 3.8

This optimization can be attributed to the opposing factors of increasing contact range and increasing holes as the UAV height is increased.

4.6 Aggregate Data Download (Adaptive Rate)

Aggregate Data Download(Adaptive Rate) is defined as the total data that the UAV can transmit reliably to the ground node while flying over at a fixed height. For $ADD - AR$, UAV is assumed to be capable of perfect rate adaption, and the resulting $ADD - AR$ can be expressed as

$$ADD - AR_h = \sum_x \frac{2 * RV_{h,x}}{v} \tag{4.8}$$

$ADD - AR_h$ is the aggregate data download for that particular height

$RV_{h,x}$ is the Rate Vector for that particular height

v is the speed of the UAV in feet/s

As in the previous case, we also assumed $v = 1$ feet/s while running simulations. After simulations, we obtain Figure 4.9

As can be seen in 4.9, the $ADD - AR$ curve is monotonic that can be attributed to the

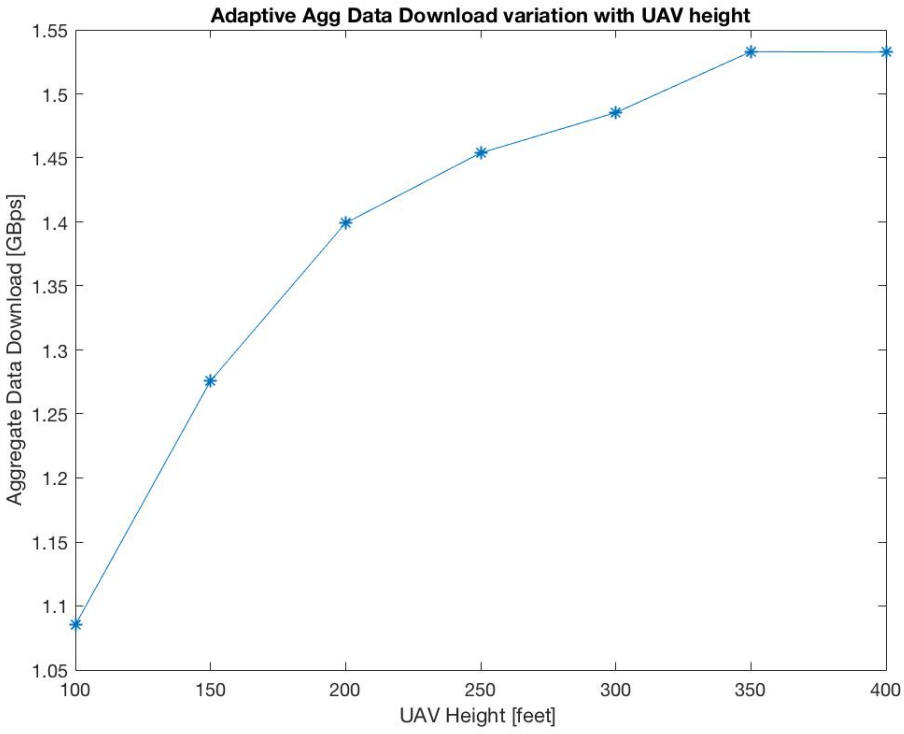

Figure 4.9: Agg. Data Downloaded variation at different UAV heights in a adaptive rate system.(The)

absence of holes in coverage for an adaptive system. As the height increases, the contact

range increases and hence follows the aggregate data download for an adaptive system.

To get a better insight into the rate dynamics of a UAV air-ground link, it is desirable to extend the above analysis to *continuous* rather than discrete rates. In the discrete analysis, rates and min SNR required were borrowed from WiFi standard (the min_SNR values listed in Table 4.1) and we used piece-wise linear interpolation(to obtain continuous min_SNR) as a function of rates.

An alternate approach would be to use the Shannon Capacity formula to derive the rates for the continuous analysis. According to Shannon Capacity Theorem for a flat (frequency non-selective) additive White Gaussian noise channel,

$$C = Blog_2(1 + SNR) \tag{4.9}$$

where
C is the capacity of the medium in bits per second, B is the channel bandwidth and SNR is the Signal-to-Noise (power) ratio over the channel.
We limit ourselves to the range of minimum SNRs listed in the Table 4.1.

We emphasize that the WiFi Rates and corresponding Shannon Capacity rates are NOT intended for direct comparison, as they pertain to two DIFFERENT channel conditions: WiFi is intended for indoor, *frequency selective fading channel* whereas the Shannon capacity is computed for a flat channel. So for appropriate comparison, the Shannon Capacity should be computed for an A-G frequency selective downlink channel model - however, this is as yet to be determined. Further, the Shannon Capacity represents an ideal system with perfect channel knowledge and Doppler compensation at the receiver - in practice, both channel and frequency estimation errors will introduce additional errors that effectively degrade the SNR and lower the link capacity. For all these reasons, the sections below are merely illustrative of the principle of the optimization (which is valid) and the rate values (and consequent ADRs) are *not* intended to be accurate of what is expected in practice.

Min SNR req (dB)	Rates(Mbps) [WiFi Legacy]	Rates(Mbps) [Shannon]
5	6	42
6	9	47
7	12	52
9	18	64
13	24	88
17	36	114
20	48	134
22	54	147

Table 4.3: WiFi Rates and Shannon Capacity rates for minimum SNR values for 802.11a standard

4.7 Rate Vector for continuous case

Using Shannon capacity formula, we get the curve in Figure 4.10 for Rate Vector for the continuous case. As one can see that the pattern of the result doesn't change but there is a significant gap in rates for a particular value of horizontal distance.

4.8 Contact Range for continuous case

One doesn't expect the contact range to change as one transitions from discrete rates to continuous rates. This is because contact range depends upon the SNR at the receiver rather than the rate. Thus, contact range metric can be used as a sanity check for the discrete to continuous transition.

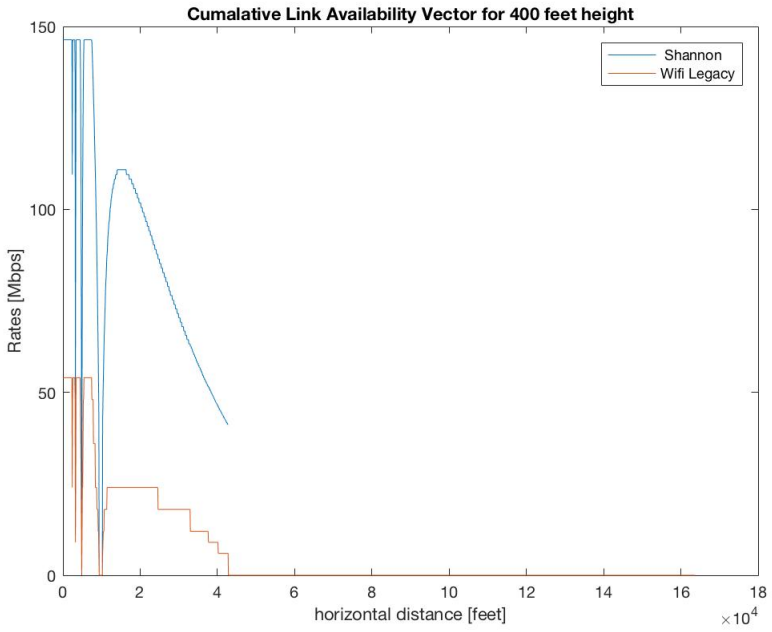

Figure 4.10: Rate Vector comparison for the continuous case and the discrete case for UAV height 400 feet (The continuous curve here has been cutoff after the point where the discrete curve goes to zero).

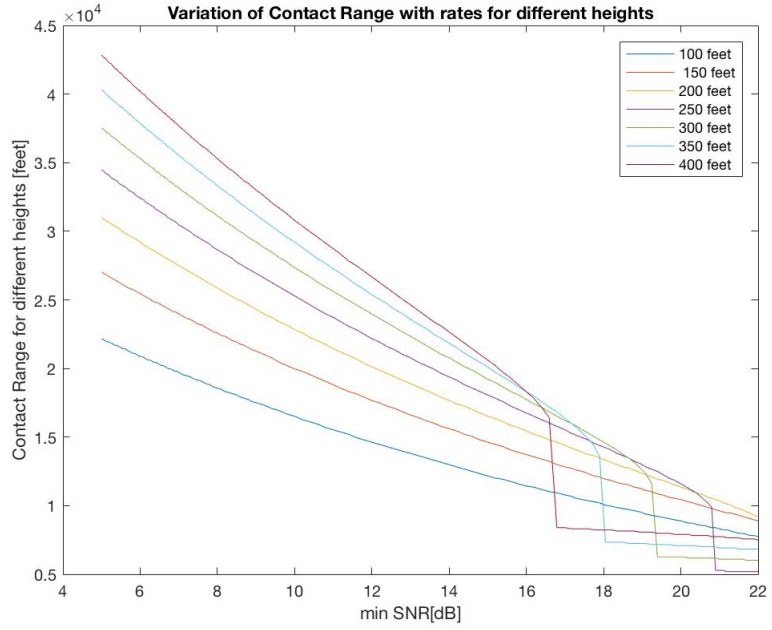

Figure 4.11: Contact Range comparison for the continuous case and the discrete case for UAV height 400 feet.)

The graphs in Figure 4.12 show that the contact range values for both the discrete and continuous case overlap. As can be seen the contact range for both discrete and continuous overlap with each other. Transitioning from discrete to continuous gives us a better understanding of how contact range varies with increasing height.

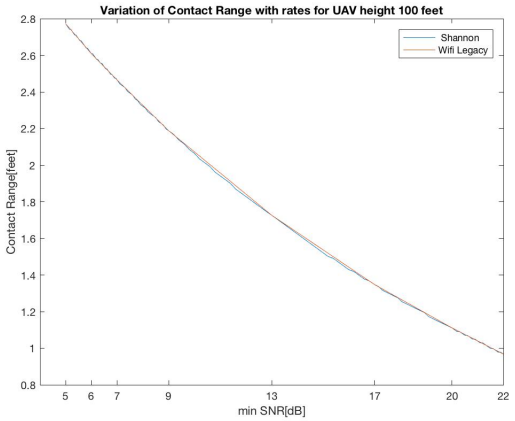

(a) Contact Range for 100 feet

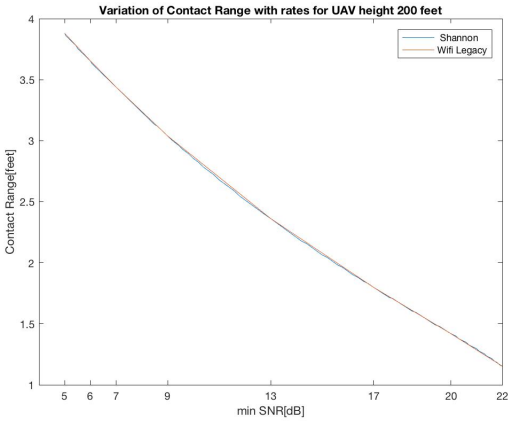

(b) Contact Range for 200 feet

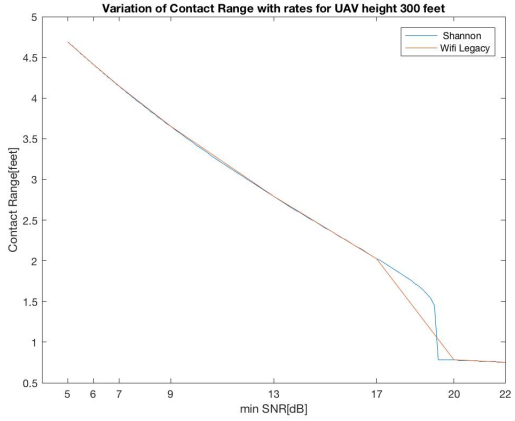

(c) Contact Range for 300 feet

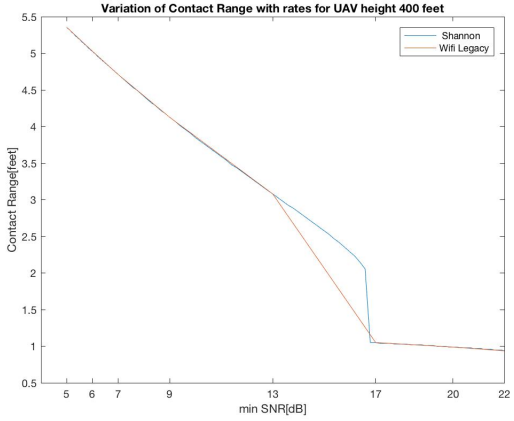

(d) Contact Range for 400 feet

Figure 4.12: Comparison of contact range for different heights for continuous and discrete rates

4.9 Aggregate Data Download for continuous case (Fixed Rate)

In this section, we will discuss the results about how the aggregate data download varies with continuous rates.The Figure 4.13 is the continuous version of the Figure 4.8 . As one can see, continuous case gives us more insight into the dynamics of the air-ground link. The optimized rate for most of the heights is no longer at a fixed rate but increases gradually with decrease in height.

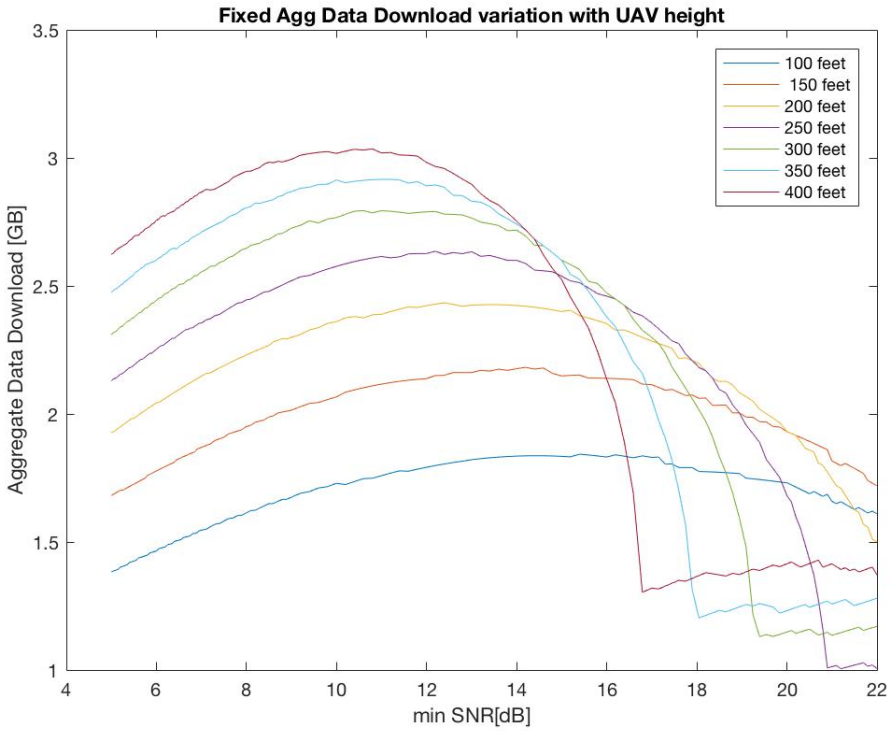

Figure 4.13: Fixed Aggregate Data Download for different heights for continuous rates

In the Figure 4.13, we can easily see that for each height, there is an optimized rate for which the aggregate data download is maximized. Comparing the continuous case with the discrete case in Figure 4.14, we see that across all the cases, the general shape of curves is

maintained as we transition from discrete to continuous case, the difference is aggregate data download is due to higher rates for the continuous case.

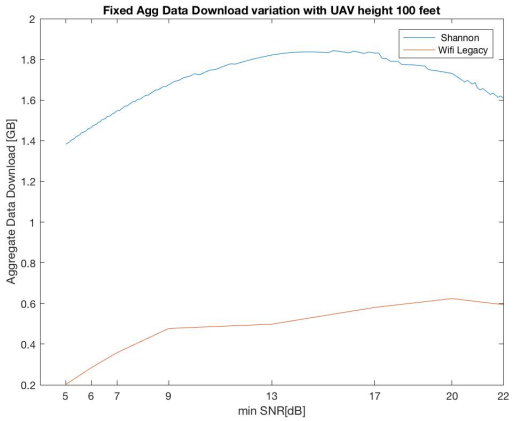

(a) Aggregate Data Download at 100 feet

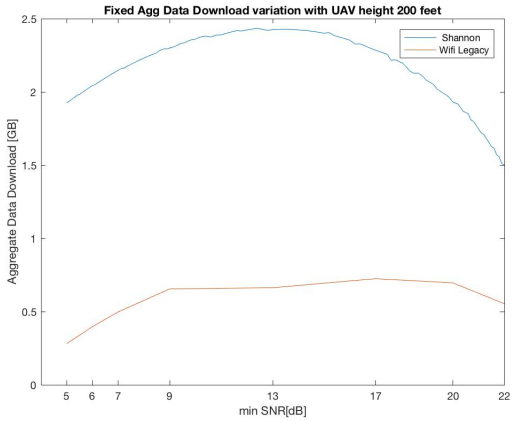

(b) Aggregate Data Download at 200 feet

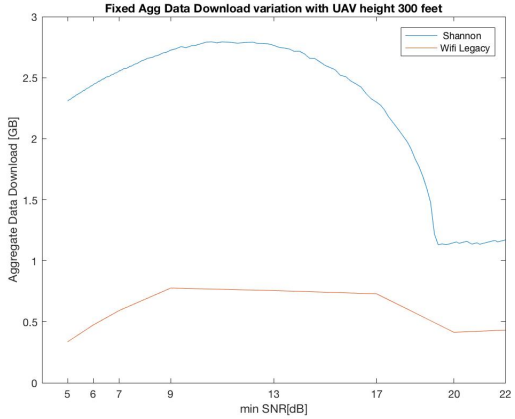

(c) Aggregate Data Download at 300 feet

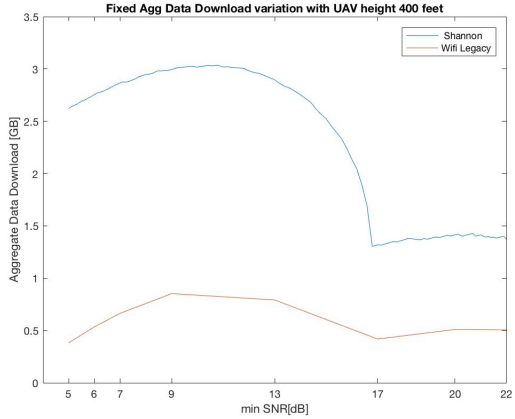

(d) Aggregate Data Download at 400 feet

Figure 4.14: Comparison of aggregate data download for different heights for continuous and discrete rates

4.10 Aggregate Data Download for continuous case (Adaptive Rate)

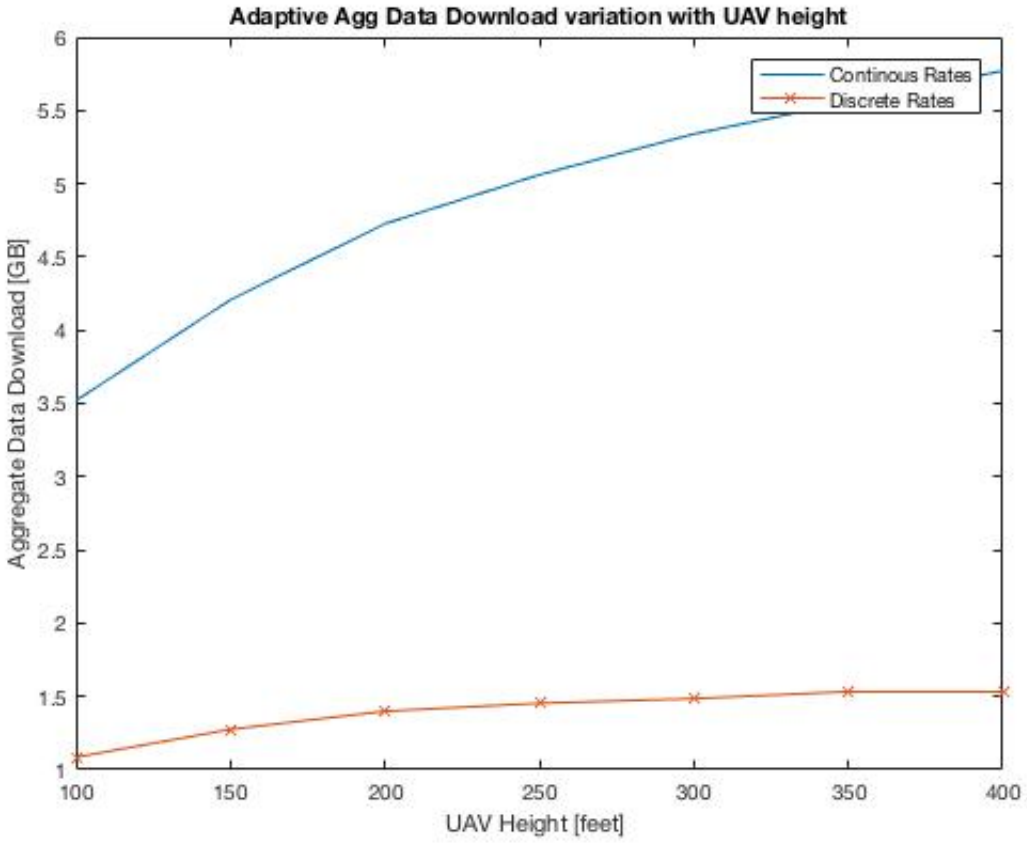

Figure 4.15: Aggregate Data Download (Adaptive System) for different heights for continuous rates

The difference for continuous rates and discrete rates in (Figure : 4.15) aggregate data download (adaptive rate) can be easily accounted for by higher rates in the continuous case for the same received signal strength.

Chapter 5

CONCLUSION

In this thesis, we developed a physics based model for UAV air-ground link, validated it using real data gathered from UAV experiments and used the model to arrive at rate optimization when a UAV flies over a single node on the ground. For realization of UAV networks, this work barely scratches the surface. Future work that builds on this effort is suggested as follows:

• On the data collection front, dynamic test data is needed wherein the UAV flies around instead of hovering at a point, in pre-determined patterns around the ground node. This data would help further understand the effect of different mobility patterns on link quality and help validate an iteration of the above model which accounts for Doppler effect and antenna radiation patterns.

• Since the presence of A-G links using unlicensed (WiFi) bands potentially adds to pollution of existing terrestrial network infrastructure of those bands, *cognitive* radio capability - whereby the A-G link can sense-and-avoid congested bands on the ground (near the ground node) is desirable. Thus the development of interference estimation and avoidance algorithms that run on the UAV - but based on uplink feedback - is needed for maintaining link quality along UAV flight path.

• A typical UAV network use-case consists of multiple UAVs flying simultaneously for coverage of a desired area of interest on the ground. Such a UAV network would need highly cognitive distributed collision avoidance algorithms as part of path planning for the UAV swarm; for this UAV-UAV communications either directly or indirectly via ground node will

be needed. Architectural considerations and design trade-offs for such scenarios are yet to be adequately explored.

BIBLIOGRAPHY

[1] Andre Spizzichino Petr Beckmann. *Scattering of electromagnetic waves from rough surfaces*. International series of monographs on Electromagnetic Waves. The MacMillan Company, 1963.

[2] David W Matolak. Unmanned aerial vehicles: Communications challenges and future aerial networking. In *Computing, Networking and Communications (ICNC), 2015 International Conference on*, pages 567–572. IEEE, 2015.

[3] Evşen Yanmaz, Markus Quaritsch, Saeed Yahyanejad, Bernhard Rinner, Hermann Hellwagner, and Christian Bettstetter. Communication and coordination for drone networks. In *Ad Hoc Networks*, pages 79–91. Springer, 2017.

[4] Sathyanarayanan Chandrasekharan, Karina Gomez, Akram Al-Hourani, Sithamparanathan Kandeepan, Tinku Rasheed, Leonardo Goratti, Laurent Reynaud, David Grace, Isabelle Bucaille, Thomas Wirth, et al. Designing and implementing future aerial communication networks. *IEEE Communications Magazine*, 54(5):26–34, 2016.

[5] David W Matolak and Ruoyu Sun. Air-ground channel characterization for unmanned aircraft systems: The hilly suburban environment. In *Vehicular Technology Conference (VTC Fall), 2014 IEEE 80th*, pages 1–5. IEEE, 2014.

[6] David W Matolak and Ruoyu Sun. Air-ground channel characterization for unmanned aircraft systems: The near-urban environment. In *Military Communications Conference, MILCOM 2015-2015 IEEE*, pages 1656–1660. IEEE, 2015.

[7] David W Matolak and Ruoyu Sun. Antenna and frequency diversity in the unmanned aircraft systems bands for the over-sea setting. In *Digital Avionics Systems Conference (DASC), 2014 IEEE/AIAA 33rd*, pages 6A4–1. IEEE, 2014.

[8] Shigeru Shimamoto et al. Channel characterization and performance evaluation of mobile communication employing stratospheric platforms. *IEICE transactions on communications*, 89(3):937–944, 2006.

[9] Wahab Khawaja, Ismail Guvenc, and David Matolak. Uwb channel sounding and modeling for uav air-to-ground propagation channels. In *Global Communications Conference (GLOBECOM), 2016 IEEE*, pages 1–7. IEEE, 2016.

[10] Jordi Romeu, Albert Aguasca, Javier Alonso, Sebastián Blanch, and Ricardo R Martins. Small uav radiocommunication channel characterization. In *Antennas and Propagation (EuCAP), 2010 Proceedings of the Fourth European Conference on*, pages 1–5. IEEE, 2010.

[11] Evşen Yanmaz, Robert Kuschnig, and Christian Bettstetter. Channel measurements over 802.11 a-based uav-to-ground links. In *GLOBECOM Workshops (GC Wkshps), 2011 IEEE*, pages 1280–1284. IEEE, 2011.

[12] Evşen Yanmaz, Robert Kuschnig, and Christian Bettstetter. Achieving air-ground communications in 802.11 networks with three-dimensional aerial mobility. In *INFOCOM, 2013 Proceedings IEEE*, pages 120–124. IEEE, 2013.

[13] Mohammad Mahdi Azari, Fernando Rosas, Kwang-Cheng Chen, and Sofie Pollin. Optimal uav positioning for terrestrial-aerial communication in presence of fading. In *Global Communications Conference (GLOBECOM), 2016 IEEE*, pages 1–7. IEEE, 2016.

[14] Markus Gruber. Role of altitude when exploring optimal placement of uav access points. In *Wireless Communications and Networking Conference (WCNC), 2016 IEEE*, pages 1–5. IEEE, 2016.

[15] Akram Al-Hourani, Sithamparanathan Kandeepan, and Simon Lardner. Optimal lap altitude for maximum coverage. *IEEE Wireless Communications Letters*, 3(6):569–572, 2014.

[16] Evşen Yanmaz. Connectivity versus area coverage in unmanned aerial vehicle networks. In *Communications (ICC), 2012 IEEE International Conference on*, pages 719–723. IEEE, 2012.

[17] Shigeru Shimamoto et al. Prediction of propagation path loss for stratospheric platforms mobile communications in urban site los/nlos environment. In *Communications, 2006. ICC'06. IEEE International Conference on*, volume 12, pages 5643–5648. IEEE, 2006.

[18] Qixing Feng, Joe McGeehan, Eustace K Tameh, and Andrew R Nix. Path loss models for air-to-ground radio channels in urban environments. In *Vehicular Technology Conference, 2006. VTC 2006-Spring. IEEE 63rd*, volume 6, pages 2901–2905. IEEE, 2006.

[19] Akram Al-Hourani, Sithamparanathan Kandeepan, and Abbas Jamalipour. Modeling air-to-ground path loss for low altitude platforms in urban environments. In *Global Communications Conference (GLOBECOM), 2014 IEEE*, pages 2898–2904. IEEE, 2014.

[20] Abhinav Jadon, Zachary T Williams, Connor Kafka, Hannah Rotta, Sumit Roy, and Christopher W Lum. A database system architecture for air-to-ground uas link characterization. In *2018 AIAA Information Systems-AIAA Infotech@ Aerospace*, page 1726. 2018.

[21] Ali Abdi, Cihan Tepedelenlioglu, Mostafa Kaveh, and Georgios Giannakis. On the estimation of the k parameter for the rice fading distribution. *IEEE Communications letters*, 5(3):92–94, 2001.

Appendix A

DIFFUSED COMPONENT FOR AN AREA

Here we consider the contribution from all the area elements lying in S instead of integrating only over the straight line elements.

$$< |\delta R|^2 >= \frac{r^2 \cot^2 \beta_0}{(\pi(h_1^2 + x^2 + y^2)(h_2^2 + (d-x)^2 + y^2)cos^4\beta)} \exp(-tan^2\beta/tan^2\beta_0)\delta x \delta y \quad \text{(A.1)}$$

where y is the vertical distance of that area element δS from the horizontal line

while for an area

$$< |\rho_d^2| >= \int_S \frac{r^2 \cot^2 \beta_0}{(\pi(h_1^2 + x^2 + y^2)(h_2^2 + (d-x)^2 + y^2)cos^4\beta)} \exp(-\frac{tan^2\beta}{tan^2\beta_0})\delta x \delta y \quad \text{(A.2)}$$

where

y is the vertical distance of the component δS from the line, as shown in Figure 2.5 .

Appendix B

WHERE TO FIND THE FILES

You can find the project related files at the following links:

- UAV Database Link

  `http://uavchannel.ee.washington.edu:8080/index/`